

# Mesoscale to Submesoscale Wavenumber Spectra in Drake Passage

CESAR B. ROCHA, TERESA K. CHERESKIN, AND SARAH T. GILLE

*Scripps Institution of Oceanography, University of California, San Diego, La Jolla, California*

DIMITRIS MENEMENLIS

*Earth Sciences Division, Jet Propulsion Laboratory, California Institute of Technology, Pasadena, California*

(Manuscript received 13 May 2015, in final form 4 December 2015)

## ABSTRACT

This study discusses the upper-ocean (0–200 m) horizontal wavenumber spectra in the Drake Passage from 13 yr of shipboard ADCP measurements, altimeter data, and a high-resolution numerical simulation. At scales between 10 and 200 km, the ADCP kinetic energy spectra approximately follow a  $k^{-3}$  power law. The observed flows are more energetic at the surface, but the shape of the kinetic energy spectra is independent of depth. These characteristics resemble predictions of isotropic interior quasigeostrophic turbulence. The ratio of across-track to along-track kinetic energy spectra, however, significantly departs from the expectation of isotropic interior quasigeostrophic turbulence. The inconsistency is dramatic at scales smaller than 40 km. A Helmholtz decomposition of the ADCP spectra and analyses of synthetic and numerical model data show that horizontally divergent, ageostrophic flows account for the discrepancy between the observed spectra and predictions of isotropic interior quasigeostrophic turbulence. In Drake Passage, ageostrophic motions appear to be dominated by inertia–gravity waves and account for about half of the near-surface kinetic energy at scales between 10 and 40 km. Model results indicate that ageostrophic flows imprint on the sea surface, accounting for about half of the sea surface height variance between 10 and 40 km.

## 1. Introduction

We investigate the governing dynamics at mesoscales to submesoscales in the upper ocean, with focus on the partition between geostrophic and ageostrophic flows. Specifically, we analyze upper-ocean kinetic energy and sea surface height (SSH) variance spectra in the Antarctic Circumpolar Current (ACC) using 13 yr of shipboard ADCP measurements in Drake Passage, complemented by satellite altimeter products and a 1-km numerical simulation with embedded tides.

This paper extends recent studies in the Gulf Stream (Wang et al. 2010; Callies and Ferrari 2013, hereinafter CF13; Bühler et al. 2014) to the Southern Ocean, where differences in dynamical regimes and scales are expected. In particular, the ACC is organized in multiple fronts (e.g., Nowlin et al. 1977), and the combination of relatively high latitude and weak stratification results in a mean

deformation radius of  $\sim 16$  km and restricts the internal wave continuum to a range of periods from  $\sim 20$  min to 14 h.

Following CF13, we employ two main diagnostics: spectral slopes of one-dimensional, along-track wavenumber spectra and the ratio of across-track to along-track kinetic energy (KE) spectra. These diagnostics are applied to in situ velocity measurements (section 3), synthetic data (section 5), and a 1-km primitive equation numerical model (section 6). Following Bühler et al. (2014), we split the one-dimensional KE spectra into rotational and divergent components and into inertia–gravity wave and geostrophic flow components (sections 3 and 6). We further separate both synthetic and model velocity into horizontally divergent and rotational parts, and we compute KE and SSH variance isotropic spectra.

We find that the upper-ocean KE spectra in Drake Passage are consistent with isotropic, interior, quasigeostrophic (QG) turbulence masked by horizontally divergent, ageostrophic flows. These ageostrophic motions are likely dominated by inertia–gravity waves and project onto horizontal scales as large as 150 km but are more significant at scales between 10 and 40 km where they account for about half of the KE. Model results

---

*Corresponding author address:* Cesar B. Rocha, Scripps Institution of Oceanography, University of California, San Diego, 9500 Gilman Dr., MC 0213, La Jolla, CA 92093.  
E-mail: crocha@ucsd.edu

indicate that horizontally divergent flows strongly imprint onto SSH.

## 2. Theoretical predictions

CF13 review the theoretical predictions for the oceanic horizontal wavenumber spectra at scales between 1 and 200 km. We summarize only the most fundamental results and emphasize the assumptions under which they are obtained.

The two turbulence paradigms invoked in the submesoscale range are interior QG and surface quasigeostrophic (SQG). Under the assumptions of statistical homogeneity and isotropy, QG turbulence theory predicts a  $k_h^{-3}$  power law for scales smaller than the forcing scale, where  $k_h = \sqrt{k^2 + l^2}$  is the isotropic horizontal wavenumber (Charney 1971; CF13). This forcing scale is generally associated with the wavelength of the most unstable mode of interior baroclinic instability (e.g., Salmon 1998). Under the same assumptions, SQG turbulence predicts  $k_h^{-5/3}$  power law at scales smaller than the forcing scale (Blumen 1978; CF13). It is not clear what would set the forcing scale of pure SQG turbulent flows in the ocean.

Shipboard transects and along-track altimeter observations permit estimation of only one-dimensional (along track) wavenumber  $k$  spectra. In geostrophic turbulence, which is nondivergent to leading-order, isotropic, and one-dimensional wavenumber spectra follow the same power law (CF13). Furthermore, along-track  $\hat{C}^v$  and across-track  $\hat{C}^u$  velocity variance spectra are related through (Charney 1971)

$$\hat{C}^u = -k \frac{d\hat{C}^v}{dk}. \quad (1)$$

Thus, if the isotropic spectrum follows a  $k_h^{-n}$  power law, then  $\hat{C}^v$  and  $\hat{C}^u$  are related through the scaling exponent  $n$ :  $\hat{C}^u = n\hat{C}^v$ . This important result was observed by Charney when comparing his predictions for geostrophic turbulence against data (Charney 1971). The ratio  $R \equiv \hat{C}^u/\hat{C}^v$  is thus a simple diagnostic that should be used together with spectral slopes to interpret one-dimensional KE spectra (CF13; Bühler et al. 2014).

Ageostrophic motions (inertia-gravity waves, mixed layer (ML) instabilities, fronts, filaments, stratified turbulence, Langmuir cells, convection cells, etc.) are also important in the submesoscale range. These flows typically flatten the spectra because they project onto small scales. A simple horizontally isotropic (empirical) model exists only for the spectrum of the internal wave continuum [the Garrett–Munk spectrum (GM); Munk 1981]. Analysis of spectra in different vertical levels and isopycnals provides insight for interpreting wavenumber

spectra dominated by different types of ageostrophic motions (CF13).

## 3. Velocity observations

### a. The ARSV *Laurence M. Gould* ADCP data

We use data from the U.S. Antarctic research and supply vessel (ARSV) *Laurence M. Gould* (LMG); the dataset is an update of the one used by Lenn et al. (2007) and by Lenn and Chereskin (2009). The LMG crosses Drake Passage approximately twice per month on its way to Palmer Station, Antarctica, and back to Punta Arenas, Chile. While steaming at  $\sim 10$  knots (kt; 1 kt =  $0.51 \text{ m s}^{-1}$ ;  $\sim 5 \text{ m s}^{-1}$ ), the LMG measures near-surface (26–300 m) currents using a hull-mounted 153.6-kHz ADCP. About 290 transects spanning 1999–2012 are available. The LMG research activities and weather conditions prohibit acquisition of data along an exactly repeating transect; there are three main routes (Lenn et al. 2007). The transects converge to about the same location in the north and the southern tip of South America and spread out poleward (Fig. 1). The ADCP data are available from the National Oceanographic Data Center (<http://ilikai.soest.hawaii.edu/sadcp/>).

The data were processed using the Common Ocean Data Access System (CODAS; Firing et al. 2012; details at <http://currents.soest.hawaii.edu/docs>). In short, the ship-relative currents are rotated from the ship frame of reference to a geographic frame using the ship's gyrocompass, corrected in post-processing using global positioning system (GPS) attitude measurements. An accurate measurement of the ship's velocity is obtained from high-precision GPS. The speed of sound at the transducers, which are immersed in an antifreeze solution, is determined from a sound velocity probe in the well. The final 5-min ( $\sim 1.25$  km), 8-m vertical bin average absolute ocean currents are accurate to  $\sim 2 \text{ cm s}^{-1}$  (appendix A). We block average the data every 5 km to make them evenly spaced, and this reduces the instrumental error to  $\sim 1 \text{ cm s}^{-1}$  (appendix A).

The ship takes  $\sim 17$  min to travel 5 km,  $\sim 5.5$  h to cover 100 km, and  $\sim 2$  days to cross the passage ( $\sim 1000$  km). We assume the ship velocity ( $\sim 5 \text{ m s}^{-1}$ ) is much larger than the along-track propagation speed of the fluctuations (the fast-tow assumption; e.g., Wang et al. 2010; CF13). For buoyancy frequencies of  $3.5 \times 10^{-3}$  and  $6.0 \times 10^{-3} \text{ rad s}^{-1}$  [Argo climatology; dataset produced by Roemmich and Gilson (2009)], the minimum period cutoff for free internal gravity waves (IW) is  $\sim 30$  min to the north and  $\sim 17$  min to the south of the Polar Front (PF). The fast-tow assumption is reasonable for high-frequency internal waves because these flows project onto small scales ( $< 50$  km). Linear first-mode internal

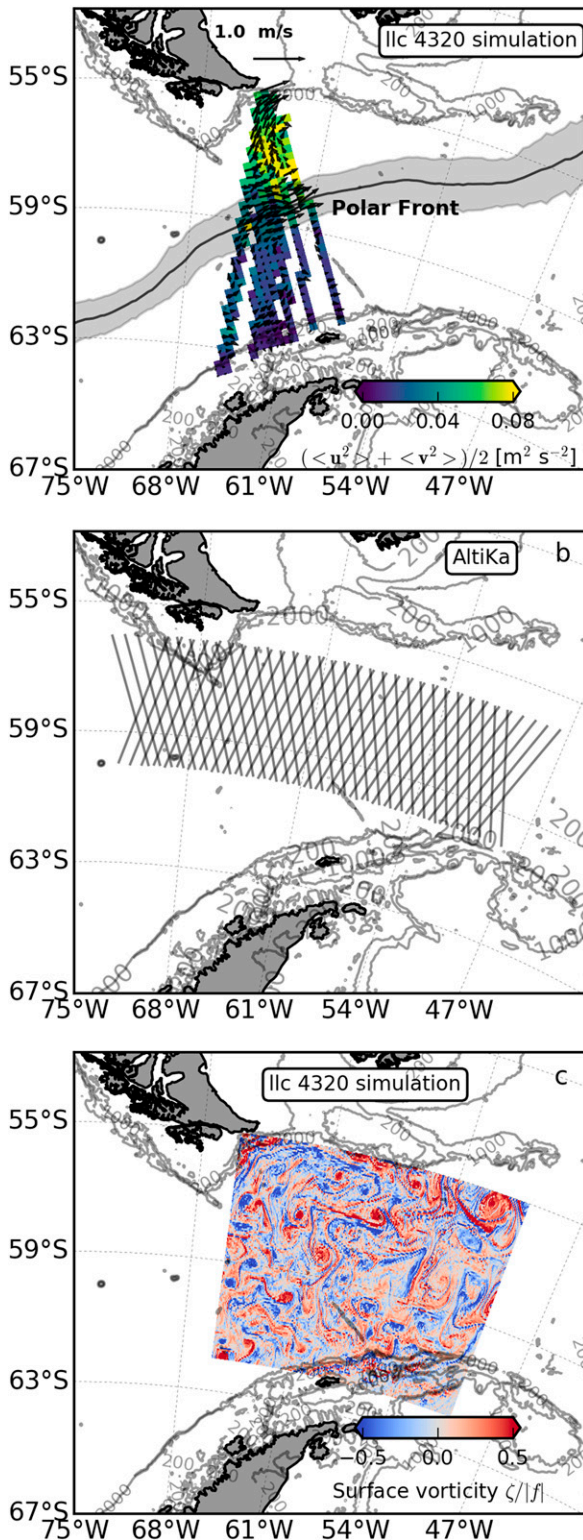


FIG. 1. (a) Gridded mean (vectors) and eddy kinetic energy (colors) from ADCP data at 26 m (uppermost bin). The black line depicts the mean position of the Polar Front [1993–2013, updated from Sallée et al. (2008)]. (b) Segments of tracks from *AltiKa* altimeter. (c) Subdomain of llc4320 simulation used in this study. Colors represent a snapshot of surface vertical vorticity normalized by the local inertial frequency.

tides have a propagation speed of  $\sim 1.5 \text{ m s}^{-1}$  (see section 7) and are likely aliased. We assess the effects of the aliasing of high-frequency motions on spectral slopes using data from a numerical model (section 6). Moreover, removing barotropic tides using estimates from a shallow-water model constrained to satellite altimeter data [TOPEX/Poseidon, version, 7.2 (TPX07.2); updated from Egbert et al. (1994)] does not change the ADCP spectral characteristics in Drake Passage; the M2 constituent dominates the tidal signal, with currents at the instrumental noise level ( $< 2 \text{ cm s}^{-1}$ ). The spectra presented here include barotropic tides.

We select 800-km-length, gap-free transects; no interpolation is performed. For each transect, at each depth, the velocity components are rotated onto an along-track/across-track coordinate system. We then remove the spatial mean and linear trend, multiply each transect by a Hanning “spectral window,” and compute the discrete Fourier transform; results are insensitive to the choice of window. We repeated the calculations mirroring each transect to make it periodic. Spectra of “periodized” transects are indistinguishable from the prewindowed spectra within error bars. The spectra are corrected for the variance removed by the window. We do not remove the low-resolution gridded mean; removing the mean changes the spectra only at scales larger than  $\sim 200 \text{ km}$ .

We form spectral estimates by multiplying the Fourier coefficients by their complex conjugate and averaging over all realizations in three different layers (26–50, 58–98, and 106–202 m). Climatologically, the mean mixed layer depth (MLD) in Drake Passage is  $\sim 40 \pm 10 \text{ m}$  in summer and  $\sim 120 \pm 30 \text{ m}$  in winter, with deeper MLDs north of the Polar Front [Argo mixed layers; dataset produced by Holte et al. (2010) and Holte and Talley (2009)]. Hence, the deepest layer considered in this study is deeper than the ML except in some realizations in winter. The weak stratification in Drake Passage, however, makes MLDs difficult to determine; different methods lead to inconsistent MLDs, particularly north of the Polar Front (Stephenson et al. 2012). Because of this caveat, we avoid discussing the results in terms of ML/pycnocline motions; we explicitly state the range of depths in each layer. Finally, Ekman currents are relatively small in Drake Passage ( $< 2 \text{ cm s}^{-1}$ ) and decay significantly in the upper 50 m (Lenn and Chereskin 2009) and therefore are likely present only in the 26–50-m layer.

Given the length of transects and resolution of the reduced data, the ADCP KE spectra resolve horizontal variability at scales spanning  $1.0 \times 10^{-1}$  cycles per kilometer (cpkm; 10 km; Nyquist scale) to  $1.25 \times 10^{-3}$  cpkm (800 km; fundamental scale) with spectral resolution of  $1.25 \times 10^{-3}$  cpkm. Formal errors are obtained

assuming that the Fourier coefficients are normally distributed (details in [appendix B](#)).

We employ a recently proposed Helmholtz decomposition to split the spectra into horizontally rotational and divergent components ([Bühler et al. 2014](#)). This decomposition assumes that the flow is statistically stationary, homogeneous, and horizontally isotropic, and the fields are periodic ([Bühler et al. 2014](#)). Under these assumptions, the unique decomposition is achieved given the across-track  $\hat{C}^u(k)$  and along-track  $\hat{C}^v(k)$  KE spectra estimated from observations (details in [appendix C](#)). Following [Bühler et al. \(2014\)](#), we further separate the rotational and divergent spectra into inertia–gravity wave and geostrophic flow components. Since no buoyancy data of sufficient quality and horizontal resolution concurrent with the ADCP data are available, we use the Garrett Munk spectrum for inertia–gravity waves (e.g., [Munk 1981](#)) to achieve the second step of the [Bühler et al. \(2014\)](#) decomposition ([appendix C](#)).

## b. Results

We present along-track wavenumber spectral estimates for along-track and across-track velocity components ([Fig. 2](#)). (In all figures, KE spectra are plotted, i.e., half of the across-track and along-track velocity variance spectra.) The spectra are steep at scales smaller than 200 km and flatten out at larger scales. Although this flattening at large scales could represent an actual change in inertial range or in the dynamics, the finiteness of the transects may account for part of this flattening. We only discuss results at scales between 10 and 200 km.

The across-track KE spectrum ( $\hat{C}^u/2$ ; the red line in [Fig. 2](#)) is just slightly flatter than  $k^{-3}$  at scales smaller than 200 km. The along-track KE spectrum ( $\hat{C}^v/2$ ; the blue line in [Fig. 2](#)) is flatter than  $\hat{C}^u$  but steeper than  $k^{-2}$ . The across-track KE spectrum  $\hat{C}^u$  is larger than the along-track KE spectrum  $\hat{C}^v$  at scales between 40 and 200 km. The two spectra  $\hat{C}^u$  and  $\hat{C}^v$  are indistinguishable below 40 km. The across-track to along-track KE ratio  $R$  varies from  $\sim 2.7$  at 170 km to  $\sim 1.0$  at 40 km. The average value of  $R$  at scales between 40 and 200 km is  $1.52 \pm 0.06$ ,  $1.52 \pm 0.06$ , and  $1.54 \pm 0.08$  for depth intervals of 26–50, 58–98, and 106–202 m, respectively.

The Helmholtz decomposition of [Bühler et al. \(2014\)](#) indicates an equipartition between rotational ( $\hat{K}^\psi$ ; the green line in [Fig. 2](#)) and divergent ( $\hat{K}^\phi$ ; the yellow line in [Fig. 2](#)) KE components at scales between 10 and 40 km. The rotational component  $\hat{K}^\psi$  dominates at scales larger than 40 km. The divergent component  $\hat{K}^\phi$  accounts for only  $\sim 10\%$  of the total KE at 200 km.

Both KE components  $\hat{C}^u$  and  $\hat{C}^v$  are more energetic across all scales in the 26–50-m depth range compared to deeper levels. However, the spectral shape does not

present any obvious depth dependence, that is, spectral slopes and the across-track to along-track ratio  $R$  are very similar across all layers. KE spectra from a 38-kHz ADCP recently installed on the *LMG* ([Firing et al. 2012](#)) suggest that these spectral characteristics extend to depths of  $\sim 1000$  m; uncertainties are much higher owing to a small number of transects, and therefore we do not discuss these results here.

To assess the effect of the Polar Front on the spectra (e.g., rendering the results statistically inhomogeneous), we computed spectra using 250-km-length subtransects north and south of the climatological PF (outside the gray shaded region in [Fig. 1](#)). These spectra resolve variability at scales spanning 10–250 km, with a resolution of  $4 \times 10^{-3}$  cpkm. While the region north of the PF is more energetic, as also seen in the physical domain ([Fig. 1](#)), the spectral shape and the across-track to along-track  $R$  are very similar in both subregions ([Fig. 3](#)). The collapse of the KE components  $\hat{C}^u$  and  $\hat{C}^v$  into a single curve seems to extend to larger scales south of the PF. More years of data are required to assess this potential difference with statistical significance.

The wave–vortex decomposition assuming the Garrett–Munk spectrum for the inertia–gravity wave component yields a consistent picture ([Figs. 2d–f](#)). In particular, the geostrophic flow component dominates at scales larger than 100 km, whereas the inertia–gravity wave component dominates at scales smaller than 40 km; at scales between 40 and 100 km, there is an approximate equipartition between vortex and inertia–gravity wave kinetic energy ([Fig. 2d](#)). The spectra of the geostrophic flow component are consistent with predictions of isotropic, interior, quasigeostrophic turbulence from scales between 10 and 200 km, with steep spectra approximately following a  $k^{-3}$  power law and the across-track component about 3 times larger than the along-track component ([Fig. 2e](#)).

The ADCP data show no seasonal variability. At scales smaller than 40 km, the KE spectra seem shallower in austral summer than in austral winter (not shown). But this result is insignificant at the 95% confidence level; there are only about 30 degrees of freedom (DOF) in the seasonal spectra; gaps are more ubiquitous in austral winter owing to high sea conditions. This apparent lack of seasonality contrasts with the Gulf Stream region, where the injection of submesoscale energy significantly flattens the KE spectrum in winter ([Callies et al. 2015](#)). An accurate assessment of seasonality in the Drake Passage spectra would require more data.

In summary, one-dimensional KE spectra in the ACC in Drake Passage are reminiscent of predictions of isotropic, interior, QG turbulence. Both KE spectra  $\hat{C}^u$  and  $\hat{C}^v$  approximately follow a  $k^{-3}$  power law between 10



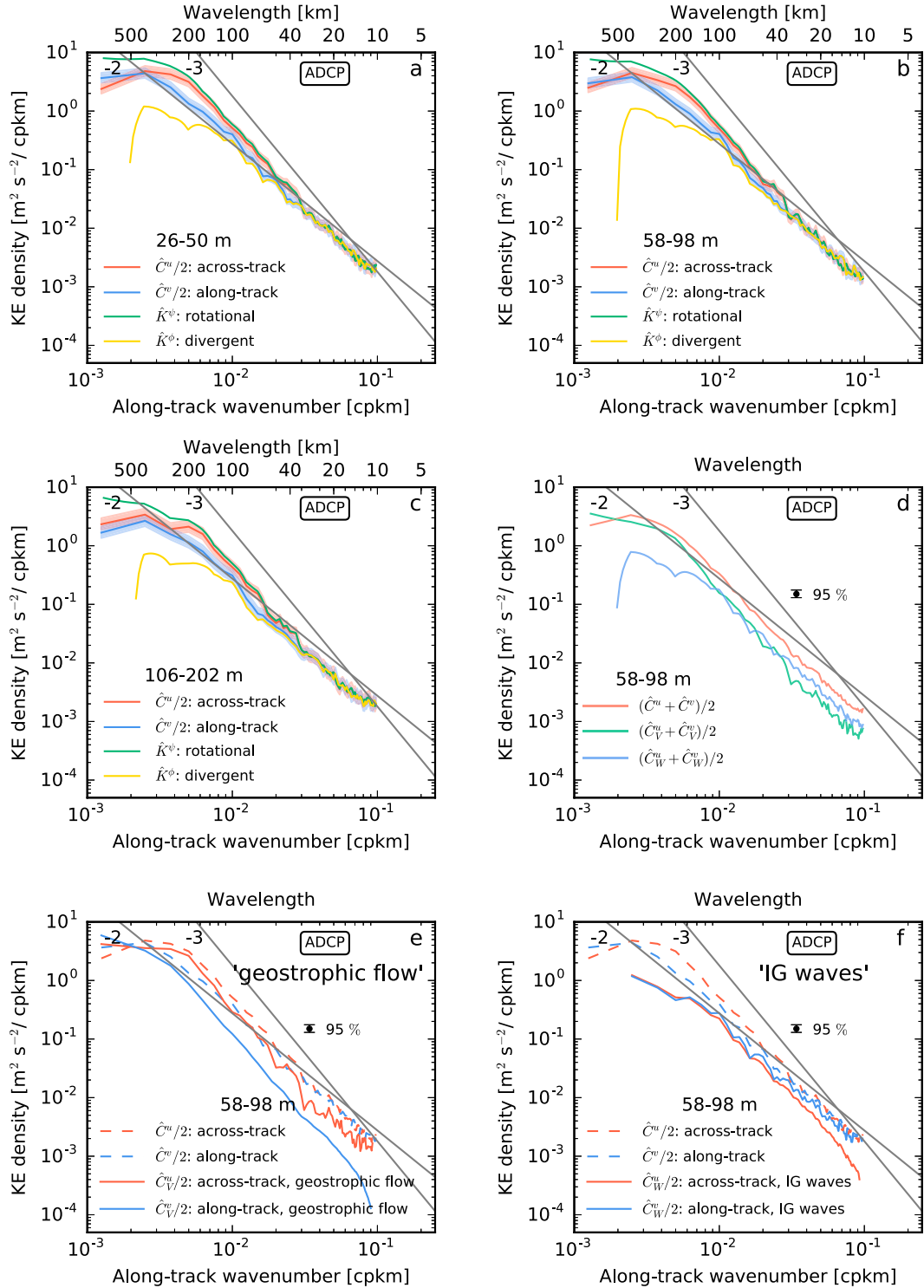


FIG. 2. ADCP KE spectra for three layers, (a) 26–50, (b) 58–98, and (c) 106–202 m, and wave–vortex decomposition for the 58–98-m layer: (d) total kinetic energy, (e) the geostrophic flow (vortex), and (f) the inertia–gravity wave components of across-track and along-track components. The figure depicts across-track (red line) and along-track (blue line) KE spectra and the spectral decomposition into horizontally rotational (green line) and divergent components (yellow line). In (a)–(c), shades represent 95% confidence limits. For reference,  $k^{-2}$  and  $k^{-3}$  curves are plotted (gray lines). In (c),(d), the confidence limits are shown as single error bars.

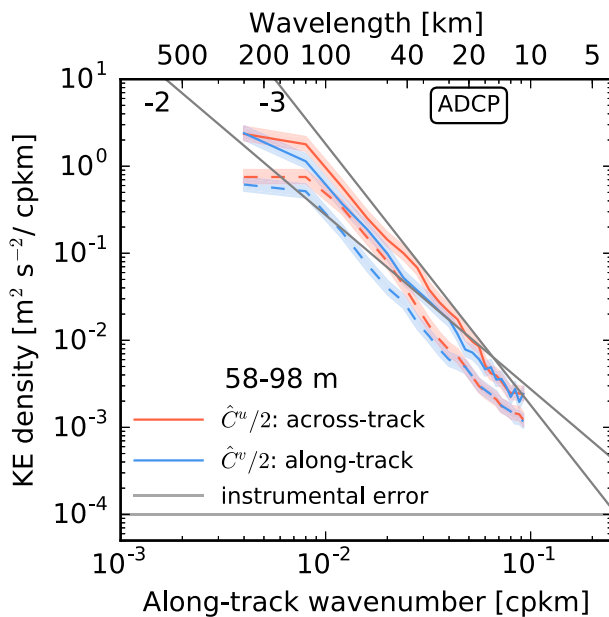


FIG. 3. ADCP KE spectra for the 58–98-m layer from subtransects to the north (solid) and to the south (dashed) of the Polar Front.

and 200 km. However,  $R \approx 1.5 < 3$ , suggesting that ageostrophic flows may be significant across this range of scales. The ageostrophic motions are likely dominated by inertia–gravity waves and are dominant at scales smaller than 40 km. We further explore this question with the aid of stochastically generated velocity fields and a numerical model (section 6).

#### 4. Satellite altimetry

##### a. The SARAL/AltiKa altimeter

Altimeter data for this analysis are drawn from the *Satellite with Argos and AltiKa* (SARAL)/Ka-Band Altimeter Radiometer (AltiKa) altimeter, which is a French and Indian mission launched in February 2013 (Verron et al. 2015). The altimeter data were produced and distributed by AVISO (<http://www.aviso.altimetry.fr/>) as part of the Ssalto ground processing segment. AltiKa was selected for this study because its Ka-band altimeter has a footprint of about 8 km, compared with 20-km footprints in the Ku- and C-band altimeters used for the TOPEX/Poseidon/Jason and ERS/Envisat series. In addition, in contrast with *Cyrosphere Satellite-2* (CryoSat-2), AltiKa flies on an exact repeat orbit, allowing us to remove the time-mean sea surface height and to compute wavenumber spectra from sea surface height anomalies. Verron et al. (2015) show that wavenumber spectra from AltiKa agree well with Jason-2 and CryoSat wavenumber spectra for length scales longer than about 70 km. AltiKa reports sea surface height data at 40 Hz,

TABLE 1. Summary of data editing criteria applied to AltiKa data.

Surface type (0 = ocean or semiencloded sea)	= 0
Number of valid points for range (count)	$\geq 20$
Root-mean-square range (m)	0 to 0.2
Sea surface height anomaly (m)	$\leq 2$
Dry troposphere correction (m)	–2.5 to –1.9
Wet troposphere correction (m)	–0.5 to –0.02
Ionosphere correction (m)	–0.1 to 0.04
Sea state bias (m)	–0.5 to 0.0025
Ocean tide (m)	$\leq 5$
Solid Earth tide (m)	$\leq 1$
Pole tide (m)	$\leq 0.015$
Significant wave height (m)	0 to 11
Backscatter coefficient $\sigma_0$ (dB)	3 to 30
Wind speed ( $\text{m s}^{-1}$ )	0 to 30
Off-nadir angle squared (degrees <sup>2</sup> )	–0.2 to 0.015
Rms ( $\sigma_0$ ) (dB)	$\leq 1$
Number of valid points to compute $\sigma_0$ (count)	$\geq 20$

equivalent to about 40 data postings every 7 km, a spatial sampling rate of about 0.177 km. The AltiKa spectra for the Drake Passage region are computed from 18 ascending and 18 descending  $\sim 460$ -km-length track segments (Fig. 1c). Thus, altimeter spectra presented here represent scales from 0.022 cpkm (460 km) to about 2.9 cpkm ( $\sim 0.35$  km).

The data are processed using an approach similar to that applied to coastal oceanography to edit data and retain small-scale signals (e.g., Durand et al. 2008; Roblou et al. 2011; Birol et al. 2010). Data are flagged as questionable if they are outside the parameter ranges specified in Table 1 or if the data quality flags are anything other than “good” [with the exception of European Centre for Medium-Range Weather Forecasting (ECMWF) data availability, for which we require a flag of two or less.]

We use the first 20 cycles of AltiKa data, which extend from 14 March 2013 to 11 February 2015. Wavenumber spectra are computed analogously to the ADCP spectra (section 3).

##### b. Results

Figure 4 shows the AltiKa along-track wavenumber spectra of SSH variance. Spectra of ascending and descending tracks are indistinguishable within error bars. The SSH variance spectra are steeper than  $k^{-4}$  at scales between 60 and 200 km. For scales smaller than 60 km, AltiKa wavenumber spectra have a stepped structure that is characteristic of nearly all altimeters (e.g., Faugere et al. 2006), with the exception of CryoSat, which has a narrow footprint. AltiKa spectra are white for scales between about 15 and 5 km and then drop off in energy before plateauing again to be white at scales smaller than 2–3 km. For scales smaller than 2–3 km, the

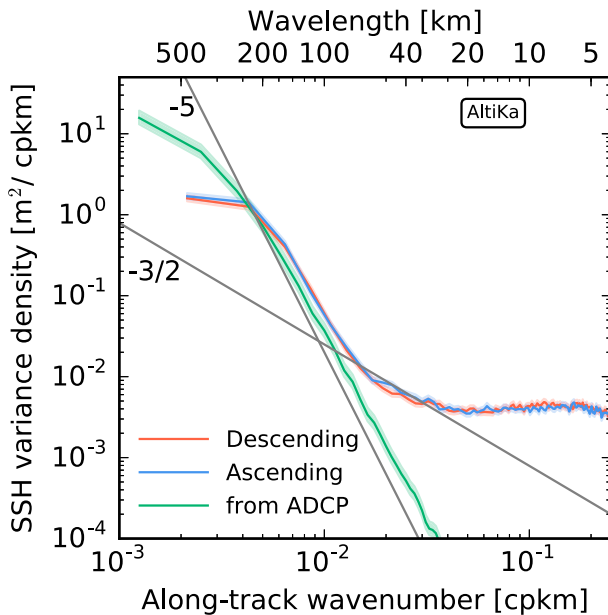


FIG. 4. *AltiKa* SSH variance along-track wavenumber spectra. For comparison, also shown is the equivalent spectrum inferred from the ADCP spectrum by assuming geostrophy.

low-energy white spectra represent instrument noise stemming from the fact that the *AltiKa* footprint is larger than the spacing between measurements, so consecutive measurements are effectively repeated looks at the same patch of ocean. The intermediate white spectrum for scales between about 5 and 15 km is referred to as a spectral hump and is associated with blooms of normalized radar backscatter  $\sigma_0$  or rain contamination (Dibarboure et al. 2014). While there have been suggestions for strategies to remove the spectral hump (e.g., Xu and Fu 2012; Zhou et al. 2015) to obtain consistent spectral slopes, we opt not to apply these approaches here and instead truncate our spectral interpretation at about 30 km.

## 5. Some experiments with synthetic data

### a. Synthetic velocity fields

We use stochastically generated velocity fields to gain insight into the interpretation of the ADCP spectra and to test the accuracy of the spectral Helmholtz decomposition (section 3). We create two-dimensional model spectra such that the associated isotropic spectra follow  $k_h^{-3}$  and  $k_h^{-2}$  power laws. These spectra are combined with Monte Carlo-generated random phases to create synthetic velocity fields [similar to the procedure employed by Rudnick and Davis (2003)]. We employ a Helmholtz decomposition to separate the two-dimensional vector fields into rotational and divergent

components (e.g., Capet et al. 2008). Because we generate the synthetic data on a two-dimensional regular grid, the Helmholtz decomposition is efficiently performed in Fourier space (e.g., Smith 2008). We calculate one-dimensional KE spectra as in section 3. We average spectra of 1000 independent velocity fields so that formal errors are insignificant.

### b. Results

As expected for a purely horizontally rotational velocity field with a  $k_h^{-3}$  isotropic spectrum, the across-track KE spectrum  $\hat{C}^u$  is 3 times larger than the along-track KE spectrum  $\hat{C}^v$ , that is,  $R = 3$  (Fig. 5a). Adding a high-pass (40-km cutoff) component of a horizontally divergent velocity field with a  $k_h^{-3}$  isotropic spectrum produces KE spectra that resemble those from the ADCP (solid yellow and green lines in Fig. 5b). The presence of divergent flows at high wavenumbers with the same level of variance as rotational flows results in  $R = 1$  at scales smaller than 40 km. At larger scales, the rotational component dominates.

No doubt, other combinations produce similar spectra. For instance, adding the velocity field with a  $k_h^{-3}$  isotropic spectrum to high-pass (40 km) divergent velocity field with a  $k_h^{-2}$  isotropic spectrum and a variance that is 25% of that of the rotational flow generates very similar spectra (dashed yellow and green lines in Fig. 5c). However, in agreement with the Helmholtz decomposition of the ADCP spectra, this simple red noise analysis suggests that in Drake Passage divergent motions alter the QG turbulence spectral characteristics. The analysis of the numerical model supports this interpretation (section 6).

The Helmholtz decomposition of the synthetic data spectra produces consistent separation into rotational and divergent components (Fig. 5). The small ( $\sim 10\%$ ) residual at scales larger than 40 km stems from the filtering process; residuals for purely rotational spectra are much smaller (Figs. 5b,c). Thus, this experiment with synthetic data verifies the robustness of the Bühler et al. (2014) decomposition, provided that the fields have stationary, homogeneous, and horizontally isotropic statistics.

## 6. A high-resolution primitive equation model

### a. The llc4320 MITgcm simulation

We analyze model output from a primitive equation (PE) global ocean simulation that resolves mesoscale eddies, internal tides, and other hydrostatic processes at scales as small as about 5 km. The llc4320 is the highest resolution ( $1/48^\circ$ ) of a hierarchy of simulations (where llc refers to latitude–longitude–polar cap). We use the 84 days of llc4320 model output spanning September

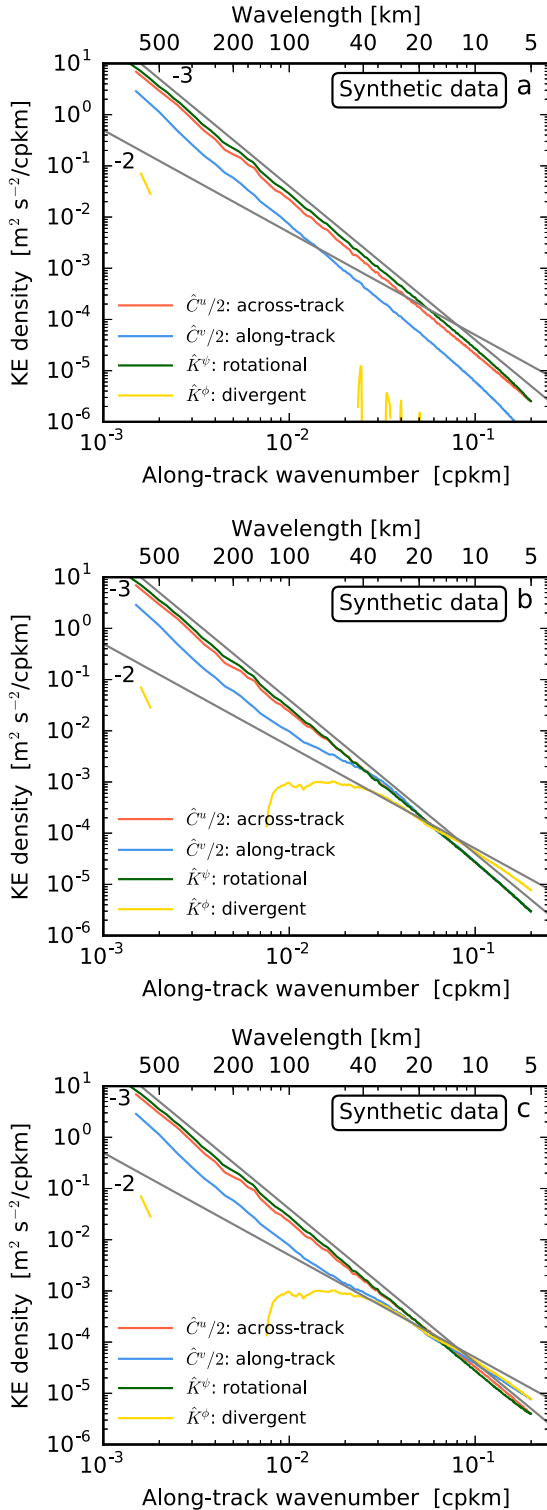


FIG. 5. Synthetic data KE spectra and its decompositions into rotational and divergent components for different combinations of horizontally rotational and divergent flows: (a)  $k_h^{-3}$  rotational flow, (b)  $k_h^{-3}$  rotational flow combined with a high-pass ( $>40$  km)  $k_h^{-3}$  divergent flow, and (c)  $k_h^{-3}$  rotational flow combined with a high-pass ( $>40$  km)  $k_h^{-2}$  divergent flow. In (c) the energy level of the divergent flow is a quarter of the energy level of the rotational flow. For reference,  $k^{-2}$  and  $k^{-3}$  curves are plotted (gray lines).

2011 through December 2011 that were available at the start of this study. The model is forced by high-frequency winds and other surface fluxes and tides (details in [appendix D](#)). The average horizontal grid spacing in Drake Passage is  $\sim 1.1$  km.

We emphasize the novelty of the global simulation analyzed here. In particular, the llc4320 simulation fully resolves mesoscale eddies and internal tides and admits some smaller-scale variability. This contrasts with the simulation analyzed by [Sasaki et al. \(2014\)](#), which has coarser resolution and neglects tidal forcing altogether. Thus, while the [Sasaki et al. \(2014\)](#) simulations represent mainly balanced dynamics, the llc4320 is able to support a more realistic mix of balanced and ageostrophic motions.

We perform our analysis in a subdomain spanning  $55^\circ$ – $62^\circ$ S,  $65^\circ$ – $50^\circ$ W ([Fig. 1](#)); we chose the eastern and polar limits to avoid sea ice contamination. Before computations, we linearly interpolate the fields onto a regular Cartesian grid ( $1.15 \text{ km} \times 1.15 \text{ km}$ ). We compute one-dimensional wavenumber spectra similarly to the ADCP, altimeter, and synthetic data estimates ([sections 3–5](#)). The spectral resolution is similar to the ADCP ([section 3](#)). The Nyquist wavenumber is  $\sim 0.5$  cpkm, but we restrict our discussion to scales larger than the model viscosity cutoff of  $\sim 5$  km (see dramatic change in spectral slopes in [Fig. 7](#)).

We also estimate horizontal isotropic wavenumber spectra from the model fields. We remove the time-mean and spatial averages of the horizontal fields. We then compute the 2D discrete Fourier transform (DFT) of these fields multiplied by a 2D Hanning window. We form the spectra by multiplying the Fourier coefficients by their complex conjugates and averaging over all realizations. We form 2D kinetic energy spectra by summing spectral estimates of the two velocity components and dividing by two. The 2D spectra are then interpolated from Cartesian to polar coordinates (in wavenumber space) and integrated in the azimuthal direction (e.g., [Richman et al. 2012](#)); in performing this interpolation, we impose low and high wavelength cut-offs of  $\sim 5$  and  $\sim 500$  km, respectively.

## b. Results

There are clear inconsistencies between model<sup>1</sup> and ADCP KE spectra ([Fig. 6](#)). The model is more than twice as energetic as the ADCP data, and, among other differences, the model spectra peaks at about  $\sim 150$  km,

<sup>1</sup> KE spectra for zonal wavenumber spectra have very similar characteristics, with meridional (across track) KE typically larger than zonal (along track) KE.



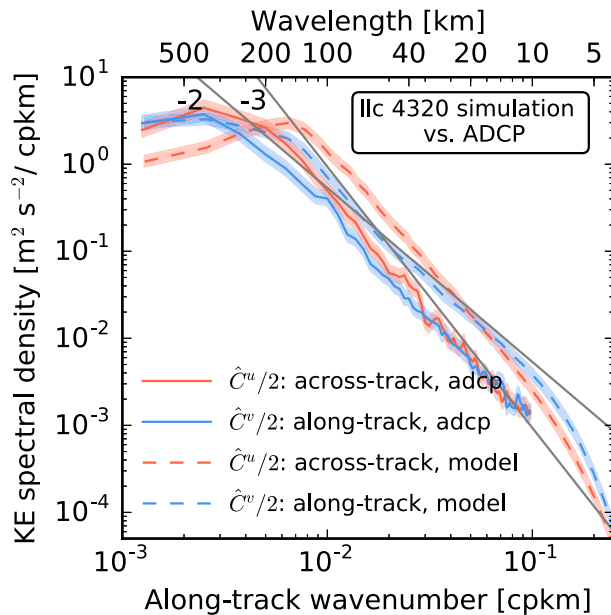


FIG. 6. Comparison between ADCP (solid) and model (dashed) spectra for the 58–98-m layer. For reference,  $k^{-2}$  and  $k^{-3}$  curves are plotted (gray lines).

whereas the ADCP  $\hat{C}^v$  peaks at  $\sim 250$  km. Besides being based on observations, statistics from the ADCP are more reliable because they are based on realizations taken over 13 yr as opposed to 84 days of model simulation. There are too few independent realizations in 84 days of simulation to produce robust spectra at low wavenumbers (see [appendix B](#)). Model KE spectra should be interpreted with these caveats.

First, we assess the degree to which the fast-tow assumption and the block averaging of the ADCP data affect the spectra. We reorder the model output so that the end of a transect represents data sampled 2 days after its beginning. To mimic the ADCP measurements, we sample transects starting half from the north and half from the south. At scales smaller than 150 km, the spectrum of this “LMG-sampled” model velocity (solid green line in [Fig. 7](#)) is indistinguishable from the spectrum of the instantaneous field (red line in [Fig. 7](#)). Similar results hold for the along-track spectrum (not shown). For instance, spectral slopes at scales between 40 and 150 km change from  $-2.51 \pm 0.12$  to  $-2.52 \pm 0.12$  for  $\hat{C}^u$  and from  $-2.51 \pm 0.12$  to  $-2.36 \pm 0.12$  for  $\hat{C}^v$ ;  $R$  changes from  $1.99 \pm 0.05$  to  $1.87 \pm 0.05$ . Block averaging the sampled fields decreases the KE at scales smaller than 20 km, slightly steepening the spectrum at high wavenumbers (dashed yellow and green lines in [Fig. 7](#)). Thus, the aliasing of rapidly evolving flows due to the ship’s finite velocity does not change significantly the spectral slopes.

Model KE spectra lack a systematic depth dependence in the upper 200 m ([Fig. 8](#)), consistent with the

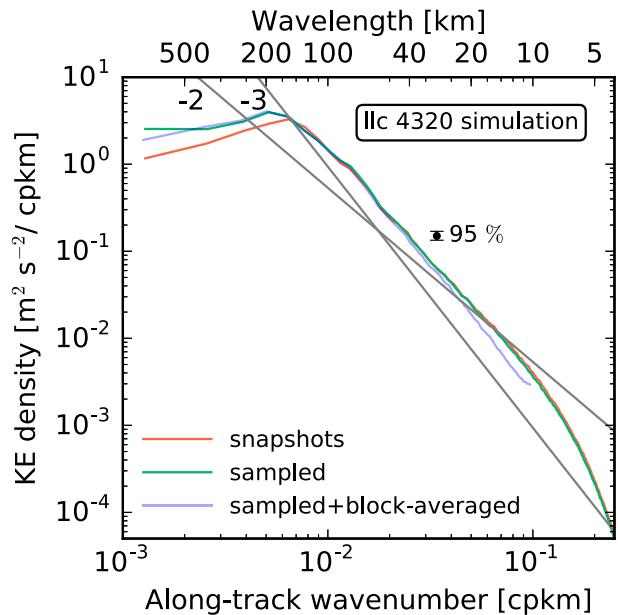


FIG. 7. Model KE spectra at the surface. The figure depicts spectra for hourly (red), and the LMG-sampled and block-averaged fields (blue and green lines). For reference,  $k^{-2}$  and  $k^{-3}$  curves are plotted (gray lines).

ADCP KE spectra ([Fig. 2](#)). The model spectra are, however, flatter than the ADCP KE spectra at scales between 10 and 200 km; the model spectral slopes are flatter than  $k^{-3}$  but steeper than  $k^{-2}$ . Also consistent with the ADCP spectra, the model along-track spectra  $\hat{C}^v$  are flatter than the across-track spectra  $\hat{C}^u$ , and the average ratio of across-track to along-track spectra  $R$  is  $\sim 1.9$  at scales between 40 and 150 km. At small scales, however,  $\hat{C}^u$  and  $\hat{C}^v$  do not collapse into a single curve. Instead, the along-track component  $\hat{C}^v$  dominates at scales smaller than 25 km, consistent with the dominance of the divergent component  $\hat{K}^\phi$  (yellow lines in [Fig. 8](#)). Conversely, the rotational spectrum  $\hat{K}^\psi$  dominates at scales larger than 40 km. The local peak in divergent KE is likely associated with low-mode internal tides (see discussion in [section 7](#)).

Removing high-frequency motions significantly changes the model KE spectral characteristics and the partition into rotational and divergent components. KE spectra of daily averaged fields (dashed lines in [Fig. 8](#)) are much steeper than the spectra of hourly fields (solid lines in [Fig. 8](#)). For instance, in the 106–202-m layer, at scales between 40 and 150 km, the spectral slope changes from  $-2.58 \pm 0.12$  to  $-2.87 \pm 0.12$  for the across-track component  $\hat{C}^u$ . Moreover, the ratio of across-track to along-track  $R$  increases from  $2.01 \pm 0.05$  for hourly velocity to  $3.12 \pm 0.10$  for daily averaged fields. The ageostrophic motions are efficiently removed by daily

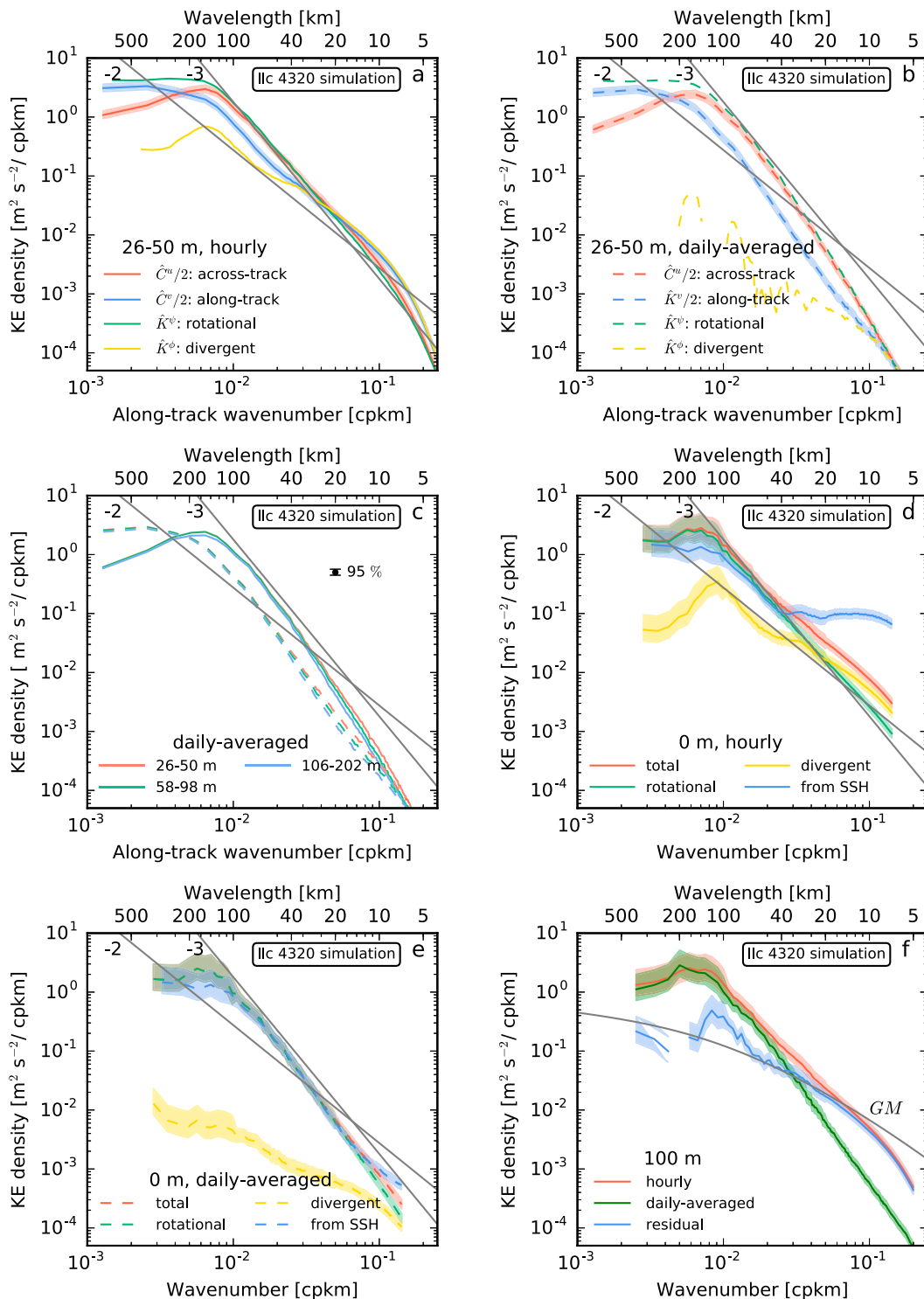


FIG. 8. Model along-track wavenumber KE spectra for the 25–60-m layer: (a) hourly; (b) daily averaged; (c) comparison of KE spectra of daily averaged fields for three layers and model isotropic KE spectra at the surface, (d) hourly and (e) daily averaged; and (f) comparison of residual spectrum with the Garrett–Munk spectrum at 100 m. In (c), solid lines represent across-track KE spectra, and dashed lines represent along-track KE spectra. Shades represent 95% confidence limits. For reference,  $k^{-2}$  and  $k^{-3}$  curves are plotted; in (f) the Garrett–Munk spectrum is plotted with 1.4 times the energy level in Munk (1981).

averaging the fields. The rotational component  $\hat{K}^{\psi}$  dominates at scales larger than 10 km. The spectra of daily, averaged velocity in the 10–150-km range have characteristics consistent with predictions of isotropic interior QG turbulence (e.g., CF13).

Conclusions based on analyses of the model isotropic spectra are consistent with results from the one-dimensional model spectra. The KE spectra of hourly fields follow a power law between  $k_h^{-2}$  and  $k_h^{-3}$  (Figs. 8d–f). Removing high-frequency motions suppresses high-wavenumber variability; the spectra of daily averaged fields are steeper than  $k_h^{-3}$ , reminiscent of QG turbulence (e.g., CF13).

A Helmholtz decomposition of the two-dimensional velocity fields shows that a significant fraction of the spectral flattening at high wavenumbers stems from horizontally divergent, ageostrophic motions. The rotational component of the KE spectrum approximately follows a  $k_h^{-3}$  power law at scales between 10 and 150 km. At the surface, the spectrum of the divergent flows peaks at about 150 km. These ageostrophic flows account for about 20% of the KE at scales between 10 and 150 km, and they contain about half of the KE at scales smaller than 40 km. Divergent flows dominate the KE at scales smaller than 20 km. High-frequency motions account for a significant fraction of divergent flows. This suggests that the divergent component is dominated by inertia–gravity waves. The KE spectra of daily averaged fields are consistent with those of rotational fields. Moreover, the residual isotropic KE spectrum (hourly minus daily averaged) has a shape consistent with the Garrett–Munk spectrum at scales between 10 and 100 km (Fig. 8f).

To further assess the interpretation that most of the ageostrophic high-wavenumber flows are accounted for by inertia–gravity waves, we calculate a horizontal wavenumber–frequency spectrum. Focusing on the high-frequency content, we estimate the spectrum every 10 days and average the results to form the spectral estimate. Because the spectrum is horizontally isotropic, we also integrate over the azimuthal direction. The results show that at scales larger than 100 km there is a gap between the energetic low-frequency (subtidal) flows and the high-frequency flows [Fig. 10 (see below)]; no clear gap exists at smaller scales. At scales smaller than 40 km, 49% of the KE is accounted for flows with frequencies larger than  $0.9f$ . Most of this high-frequency energy is spread about the dispersion relationship of linear inertia–gravity waves (Fig. 10).

The KE spectrum computed from velocities diagnosed from SSH is consistent with surface velocity fields at scales larger than 40 km (Fig. 8d). At scales between 10 and 40 km, the KE spectrum of velocities computed from SSH is essentially white noise because

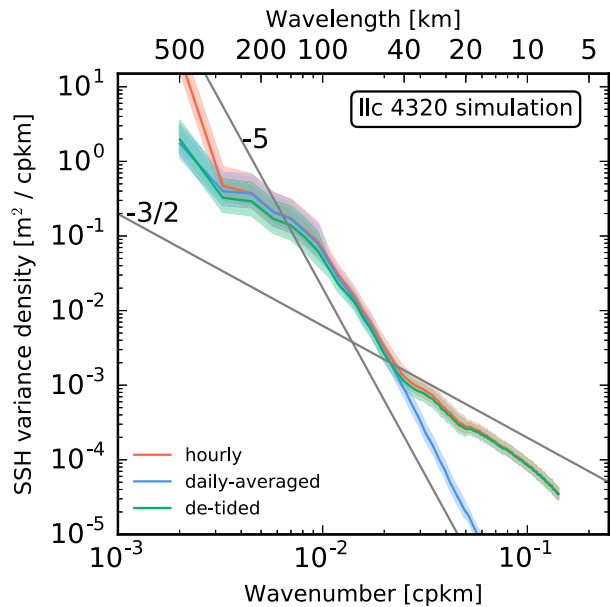


FIG. 9. Isotropic wavenumber SSH variance spectrum. Shades represent 95% confidence limits. For reference,  $k^{-3/2}$  and  $k^{-5}$  curves are plotted (gray lines).

geostrophy does not hold for a significant fraction of the flows at these scales. Daily averaging the SSH fields suppresses ageostrophic motions, and the KE spectrum of velocities diagnosed from SSH approximately follows a  $k_h^{-3}$  power law, consistent with the spectrum of daily averaged velocities.

The shape of the KE spectra and the partition of the flow into rotational and divergent components show little depth dependence in the upper 1000 m. The main difference is that KE spectra at 1000 m (not shown) lack the sharp peak in the spectra of divergent motions at 100 km. The spectra of daily averaged fields show a small, but statistically insignificant, depth dependence (the spectra steepens at depth; see Fig. 8c).

Similar conclusions are drawn from SSH variance spectra (Fig. 9). The variance spectrum of hourly SSH fields is roughly consistent with predictions of isotropic interior QG turbulence at scales between 40 and 150 km. The SSH variance spectrum dramatically flattens at scales smaller than 40 km. Removing high-frequency flows by daily averaging the SSH fields suppresses high-wavenumber variance (Fig. 9). The spectra of daily averaged SSH approximately follow a  $k_h^{-5}$  power law between 10 and 150 km.

To assess the fraction of SSH variance due to coherent tides, we remove tidal frequencies using t-tide (Pawlowicz et al. 2002). In Drake Passage, tidal motions dominate the SSH variability, accounting for 50%–80% of the SSH variance. But the majority of this variability is due to barotropic tides, which project onto scales

larger than 200 km. There is insignificant tidal variability at scales smaller than 40 km (Fig. 9). Similar results are obtained by detiding the velocity fields (not shown). Hence, most of the high-wavenumber ageostrophic variability is likely due to a continuum of inertia–gravity waves and other ageostrophic flows.

## 7. Discussion

In strong baroclinic currents, the stretching term associated with the mean flow vertical shear dominates the quasigeostrophic potential vorticity (QGPV) gradient (e.g., Tulloch et al. 2011). Background available potential energy is converted into eddy KE through baroclinic instability locally in wavenumber–frequency space (the fastest growing mode dominates the conversion). In QG turbulence, the KE spectrum is then filled through triad interactions that result in an inverse energy cascade and a direct enstrophy cascade (e.g., Salmon 1998).

Based on a local, linear, QG stability analysis of climatological fields, Tulloch et al. (2011) classified both the ACC and the Gulf Stream in the same regime. This regime is characterized by a deep reversal in the QGPV gradient that drives interior QG baroclinic instabilities. In Drake Passage, we estimate the mean deformation radius from cDrake in situ observations (Chereskin et al. 2012) to be  $\sim 16$  km and the wavelength of the most unstable modes to be about 188 km (see appendix E). This is roughly consistent with estimates of Tulloch et al. (2011) based on very smooth climatologies, which suggest that the most unstable mode is about twice the deformation scale:  $L_{\text{inst}} = 2 \times 2\pi \times 16 \approx 200$  km. This forcing scale (or injection scale) is roughly the lowest wavenumber in the range of scales analyzed in our study.

Indeed, the emerging picture of the ACC in Drake Passage has similarities to the one drawn from the ADCP observations in the Gulf Stream (Wang et al. 2010; CF13). As in the Gulf Stream, the spectral slopes  $2 < n < 3$  are reminiscent of predictions of isotropic QG turbulence in the enstrophy inertial range (Wang et al. 2010; CF13). The ratio of across-track to along-track KE energies  $R$  significantly departs from the expectations of isotropic interior QG turbulence ( $R = n$ ; Charney 1971; CF13) at scales as large as  $\sim 150$  km. The inconsistency between theoretical prediction and the ADCP KE spectra is dramatic in the 10–40-km subrange where we find  $R \approx 1$ .

The decomposition of the KE spectra into horizontally rotational and divergent components in conjunction with analyses of stochastically generated velocity fields and data from the llc4320 simulation indicate that horizontally divergent flows are responsible for the difference between  $R$  and  $n$ . This interpretation is

consistent with the analyses of the ADCP data in physical space; the eccentricity of variance ellipses is typically small (Lenn et al. 2007), and thus it is unlikely that the fact that  $R < 3$  stems from anisotropies in the flow. However, Lenn et al. (2007) interpret the fact that the ratio of along-passage to across-passage (their coordinate system that is roughly across track/along track) velocity variance spectrum is larger than 1 as evidence for anisotropy. While anisotropies may also lead to  $R \neq 1$ , differences in one-dimensional KE spectra are expected in isotropic QG turbulence (Charney 1971; CF13). If large-scale eddy flows were markedly anisotropic in Drake Passage, this characteristic would remain in the daily averaged fields. Instead, model spectra of daily averaged velocity are consistent with predictions of isotropic interior QG turbulence (e.g., CF13).

The SSH variance spectrum from the *AltiKa* altimeter is consistent with ADCP and model spectra at scales larger than about 70 km. At scales between 70 and 200 km, the *AltiKa* spectrum in Drake Passage is consistent with TOPEX/Poseidon/*Jason* spectra in other high eddy kinetic energy regions (Le Traon et al. 2008; Xu and Fu 2012). We interpret this steep spectral slope as consistent with predictions of isotropic interior QG turbulence. The change in slope in the *AltiKa* spectrum at scales between 30 and 70 km is consistent with the shallowing of the model SSH variance spectrum due to ageostrophic flows (see Figs. 4, 9). However, the *AltiKa* spectral flattening should be interpreted with care at these small scales. We were unable to distinguish between noise and ageostrophic flows based only on along-track snapshots of SSH.

In Drake Passage, ageostrophic motions appear to be dominated by inertia–gravity waves. The wave–vortex decomposition of Bühler et al. (2014) using the Garrett–Munk spectrum of inertial–gravity waves yields consistent results. Of course, the validity of this decomposition depends strongly on the assumptions that the Garrett–Munk spectrum accurately depicts the wave fields in the Southern Ocean. Previous studies suggest a rough universality of the Garrett–Munk spectrum (Munk 1981), and the residual numerical model isotropic KE spectrum (hourly KE spectrum minus daily averaged spectrum) is also roughly consistent with the shape of the Garrett–Munk spectrum (Fig. 9). Furthermore, a significant fraction of the high-wavenumber KE is spread about the dispersion relationship of linear inertia–gravity waves (Fig. 10). Thus, while all these assumptions are not strictly true, it is unlikely that the Bühler et al. (2014) decomposition is misleading, particularly in the low- and high-wavenumber ends of the spectrum where geostrophic flows and inertia–gravity waves dominate, respectively.



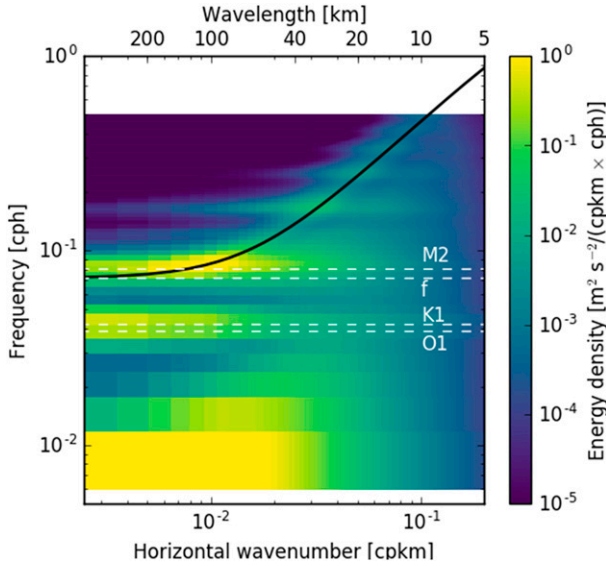


FIG. 10. Horizontal wavenumber frequency spectrum of KE at 100 m. The solid line is the dispersion relationship for inertia-gravity waves integrated over vertical wavenumber, and the dashed lines indicate tidal and inertial frequencies. The inertial frequency is based on the mean latitude of the domain (about 59°S).

The Garrett–Munk spectrum does not account for tidal peaks. We can estimate the horizontal scale of the  $n$ th-mode internal tide using the hydrostatic linear inertia–gravity wave dispersion relationship:

$$L_n \sim 2\pi \times R_n / \sqrt{\omega^2/f_0^2 - 1}, \quad (2)$$

where  $R_n$  is the  $n$ th deformation radius;  $\omega$  and  $f_0$  are the tidal and the inertial frequencies. For the first-mode  $M_2$  tide  $\omega \approx 1.41 \times 10^{-4} \text{ rad s}^{-1}$ , and using the mean inertial frequency  $f_0 \approx 1.25 \times 10^{-4} \text{ rad s}^{-1}$ , we obtain  $\sim 146$  and  $\sim 195$  km for model and cDrake stratification, respectively. In the model, this is the peak in the KE spectra of horizontally divergent motions (the solid yellow line in Fig. 8a) and peak in the residual spectrum (the solid blue line in Fig. 8f).

The low-mode internal tides are significantly anisotropic, and the Bühler et al. (2014) decomposition may not be very accurate at that peak. In the model, the low-mode internal tides are generated on the continental slope off the southern tip of South America. An animation of vertical velocity shows that the low-mode internal tides are significantly scattered and distorted as they propagate into the passage, generating small-scale inertia–gravity waves that are more isotropic. Indeed, tidal flows account for an insignificant fraction of the ageostrophic variability at scales smaller than 40 km.

That ageostrophic motions may contribute significantly to the upper-ocean variability should not be a

surprise (e.g., Ferrari and Wunsch 2010; Wunsch 2013). Analysis of a global model with embedded tides suggests that high-frequency motions significantly flatten the near-surface spectra (Richman et al. 2012). By comparing spectra of high-pass and low-pass fields in different regions, Richman et al. (2012) argue that internal tides dominate the ageostrophic signal in SSH; the effect of ageostrophic motions are dramatic in well-known internal tide hot spots (e.g., in the vicinity of the Hawaiian archipelago; Richman et al. 2012). The present study indicates that ageostrophic flows also contribute significantly to the upper-ocean variability in high eddy KE regions. Moreover, the ageostrophic signal is largely nontidal at scales smaller than 40 km.

Interior geostrophic turbulence and inertia–gravity waves coexist at scales between 10 and 200 km, with the former dominating at scales larger than 100 km and the latter dominating at scales smaller than 40 km. In both ADCP and model KE spectra there is no plateau suggesting separation of QG turbulence from ageostrophic flows. Indeed, there is an approximate equipartition of the KE between vortex and wave components between 40 and 100 km. A gap could appear in the vertical wavenumber spectra of other quantities such as shear and strain variance (Pinkel 2014). The extent to which inertia–gravity waves and geostrophic flows interact to generate the observed spectra deserves further investigation.

There is growing observational evidence for the importance of other mixed layer intensified motions that develop in response to mesoscale straining; these mixed layer submesoscale motions are ubiquitous features of the upper ocean (e.g., Shcherbina et al. 2013). These flows scale roughly with mixed layer deformation radius (Thomas et al. 2008). In Drake Passage, we estimate  $L_{ml} = N_{ml}H_{ml}/|f_0| = 100 \times 2.8 \times 10^{-3}/1.25 \times 10^{-4} \approx 2.3$  km, where  $N_{ml}$  is the mean stratification frequency in the mixed layer from Argo climatology [dataset produced by Roemmich and Gilson (2009)] and  $H_{ml}$  is the mean mixed layer depth. Given this scale, it is likely that mixed layer submesoscales are only marginally, if at all, resolved by the ADCP data and the llc4320 simulation. Moreover, the lack of statistically significant depth dependence in the shape of both model and ADCP spectra and in the partition into rotational and divergent components suggest that mixed layer–confined flows are subdominant in the range of scales considered here.

As discussed in section 3, the ADCP data do not fully resolve the horizontal spectrum of inertia–gravity waves. While the exercise of sampling the model results to mimic the ADCP data suggests insignificant aliasing, block averaging the data slightly reduces the variance at high wavenumbers, and inertia–gravity waves may be only marginally resolved by the ADCP

data (section 6). While block averaging the ADCP data every 5 km may slightly steepen the KE spectra, the spectra would be unlikely to change from  $k^{-5/3}$  to  $k^{-3}$ . Indeed, the model spectra are inconsistent with SQG turbulence, which predicts flat KE spectra at the surface ( $k^{-5/3}$ ) and steeper spectra at deeper levels (CF13; see also appendix F).

Finally, the upper ocean is also host to many other flows. For instance, stratified turbulence may be important in the pycnocline, whereas Langmuir cells may take place in the upper part of the mixed layer. These “sub-submesoscale” flows (<1 km) are not resolved by our dataset. The extent to which these flows change the high-wavenumber end of the submesoscale range remains to be investigated.

## 8. Conclusions

We remind the reader of the limitations of this study. Ocean turbulence theories, the Bühler et al. (2014) decomposition, and the Garrett–Munk spectrum assume stationary, horizontally homogeneous and isotropic statistics; we also make the first two assumptions when averaging multiple realizations to produce the spectral estimates. In applying the second step of the Bühler et al. (2014) decomposition, we assumed that the Garrett–Munk spectrum provides an accurate representation of the inertia–gravity wave spectrum in the Southern Ocean. None of these assumptions are strictly true in the real ocean. Furthermore, the formal, statistical error bars shown with the spectra do not account for unresolved variance in the ADCP or altimeter data nor do they allow for missing physics in the model. Nevertheless, this study provides the first robust description of the upper-ocean mesoscale to submesoscale horizontal wavenumber spectra in the Southern Ocean and attempts to explore its partition into geostrophic flows and inertia–gravity waves. Our main conclusions are as follows:

- At scales between 10 and 200 km, the upper-ocean (0–200 m) horizontal wavenumber spectra in Drake Passage are consistent with isotropic interior QG turbulence masked by unbalanced motions.
- *AltiKa* altimeter data do not fully resolve all scales from 10 to 200 km but are consistent with ADCP spectra for scales larger than about 70 km.
- In Drake Passage, ageostrophic motions account for about half of the near-surface kinetic energy at scales between 10 and 40 km and are likely dominated by inertia–gravity waves.
- Model results indicate that ageostrophic motions significantly imprint on the surface, accounting for about half of the sea surface height variance at scales between 10 and 40 km.

Isotropic interior QG turbulence theory appears to be a relevant framework near strong baroclinic currents (Wang et al. 2010; CF13; this study), although it is only part of the governing dynamics at mesoscales to sub-mesoscales. A robust assessment of the eddy variability in terms of turbulence theories, however, requires evaluation of the transfers of energy and enstrophy across different scales (e.g., Richman et al. 2012). The present observations prohibit estimation of such diagnostics.

The present results have implications for high-resolution altimeters, for example, the upcoming Surface Water and Ocean Topography (SWOT) mission. Unbalanced flows may upset the estimation of  $O(10)$ -km-resolution surface geostrophic velocities with low noise-to-signal ratios. That is, the high-wavenumber sea surface height variability may represent a different, ageostrophic, physical regime. This problem deserves further investigation.

*Acknowledgments.* We had stimulating discussions with William R. Young. Comments by Young, Jörn Callies, Greg Wagner, and two reviewers helped to improve the first draft. Discussions with Callies led to appendix C. This study was funded by the NASA Ocean Surface Topography Science Team (NNX13AE44G), SWOT Science Definition Team (NNX13AE85G), and the NSF Polar Programs (PLR-1341431; PLR-1141922). CBR was partially supported by NSF (OCE 1357047). We are grateful to the captain and crew of the ARSV *Laurence M. Gould* and to the Antarctic Support Contractor for their excellent technical and logistical support on the cruises. Sharon Escher, Eric Firing, and Jules Hummon have been invaluable for their contribution to the ADCP data collection, processing, and editing. Caroline Papadopoulos downloaded and archived the model data onto our servers, and Jinbo Wang helped with code for efficiently loading the model data in Python. We are also grateful to C. Hill and G. Forget at MIT; C. Henze and B. Nelson at NASA Advanced Supercomputing (NAS); A. Chaudhuri at Atmospheric and Environmental Research (AER); and the many other MITgcm developers, NAS computer scientists, and SGI engineers that made possible and available the high-resolution model output.

The ADCP and altimeter datasets used in this project are available from the data servers cited throughout the text; the control files for the llc simulations are also available from the MITgcm repository. Plotting scripts, supplementary materials, and data (e.g., ADCP spectra) are openly available online (at [https://github.com/crocha700/dp\\_spectra](https://github.com/crocha700/dp_spectra)).

## APPENDIX A

## ADCP Error Budget

The accuracy in the ADCP relative velocity is estimated as (RD Instruments 1996)

$$\sigma_{\text{rel}} = \frac{1.6 \times 10^5}{F \times D \times \sqrt{N}}, \quad (\text{A1})$$

where  $F$  is the frequency of the sonar,  $D$  is the size of the vertical bin, and  $N$  is the number of pings averaged to form the relative velocity estimate. For the LMG ADCP,  $F = 153.6 \text{ kHz}$  and  $D = 8 \text{ m}$ . The ADCP sampling rate is  $1 \text{ Hz}$ ; thus,  $N = 300$  for 5-min averages. Hence,  $\sigma_{\text{rel}} \sim 7.5 \times 10^{-3} \text{ m s}^{-1}$ .

The GPS system has an accuracy of  $\sim 5 \text{ m}$ . Averaging over  $\Delta t = 5 \text{ min}$  yields an estimate for the error stemming from position accuracy of  $\sigma_{\text{pos}} = \sqrt{2} \times 5 / \Delta t \approx 2.4 \times 10^{-2} \text{ m s}^{-1}$ . Hence, the random error in the 5-min absolute horizontal velocity estimates is

$$\sigma_{\text{abs}} = \sqrt{\sigma_{\text{rel}}^2 + \sigma_{\text{pos}}^2} \approx 2.5 \times 10^{-2} \text{ m s}^{-1}. \quad (\text{A2})$$

Block averaging the 5-min data every 5 km ( $\sim 17 \text{ min}$  for a mean ship velocity  $V_{\text{ship}} = 10 \text{ kt} \approx 5 \text{ m s}^{-1}$ ) decreases the error as  $1/\sqrt{17/5} \approx 0.54$ . Thus, the instrumental error in the 5-km absolute velocity is  $\sim 1.35 \times 10^{-2} \text{ m s}^{-1} \sim O(1) \text{ cm s}^{-1}$ .

Besides random error, there is also a potential bias stemming from errors in the gyroscope. This error is corrected when processing the raw data in CODAS using the GPS heading that appears to be accurate to  $< 0.1^\circ$  (see appendix 3 of Firing et al. 2011). An estimate of this bias is then  $\sigma_{\text{bias}} = V_{\text{ship}} \times \sin(0.1^\circ) \approx 7.2 \times 10^{-3} \text{ m s}^{-1} \sim O(1) \text{ cm s}^{-1}$ . It is likely that this bias does not significantly affect spectral slopes and the ratio of across-track to along-track KE spectra.

## APPENDIX B

## Confidence Limits in Spectral Estimates

To estimate confidence limits (CLs), we assume that the Fourier coefficients are normally distributed and consequently that their magnitudes squared are  $\chi^2$  distributed (e.g., Bendat and Piersol 2010). The average separation between the end of one transect and the start of the next is  $\sim 13 \text{ days}$ . This is about the velocity decorrelation time scale in Drake Passage as estimated from deep moorings (Bryden 1979). In the upper ocean, velocity decorrelates faster; the integral time scales estimated from the model are  $< 8 \text{ days}$ . Given that less

than 30% of consecutive transects are separated by less than 6 days, and only 10% by less than 4 days, we consider each transect as an independent realization of the spectrum (see also Lenn et al. 2007). We consider only one independent realization per transect within each layer. Employing these criteria yields  $N = 116$ , 119, and 55 independent realizations of the spectrum for the 26–50-, 58–98-, and 106–202-m layers, respectively; gaps are ubiquitous in deeper bins. For altimetry, we assume each satellite pass to be independent. We consider 32 ascending and 32 descending ground pass segments and make use of the first 20 cycles of the *AltiKa* mission, and after removing satellite passes with flagged data, this results in  $N = 518$  for descending ground tracks and  $N = 519$  for ascending ground tracks.

To calculate the number of independent realizations of one-dimensional llc4320 simulation spectral estimates, we first estimate time and length integral scales from autocorrelation functions for daily averaged fields (e.g., Bendat and Piersol 2010). We obtain, on average,  $\sim 34$  and  $\sim 45 \text{ km}$  for decorrelation length scales of zonal and meridional components, respectively; the mean time scales are  $\sim 7$  and  $\sim 6 \text{ days}$ . Using the largest/longest spatial/time scale yields 200 independent realizations of the one-dimensional spectrum.

As for the isotropic spectra, considering the largest time scale yields 10 independent realizations of the 2D spectra. Given the redness of the spectra, this is likely an underestimate for relatively small-scale motions; high-wavenumber motions are typically faster than low-wavenumber ones. (The exceptions are tides, which have relatively low horizontal wavenumbers but evolve relatively fast.) We then further assume that motions in the 20–100- and 10–20-km subranges decorrelate on 2.5 and 1 days, respectively. These criteria yield 10, 40, and 80 independent realizations of the isotropic spectra for above 100-, 20–100-, and 10–20-km subranges, respectively.

## APPENDIX C

## Details of the Helmholtz and Wave–Vortex Decompositions of One-Dimensional KE Spectra

To decompose the across-track  $\hat{C}^u/2$  and along-track  $\hat{C}^v/2$  kinetic energy spectra into rotational  $\hat{K}^\psi$  and divergent  $\hat{K}^\phi$  components, we first compute the spectral functions  $\hat{F}^\psi$  and  $\hat{F}^\phi$  by solving the coupled system (Bühler et al. 2014):

$$k \frac{d\hat{F}^\phi}{dk} - \hat{F}^\psi = -\frac{\hat{C}^v}{2}, \quad \text{and} \quad k \frac{d\hat{F}^\psi}{dk} - \hat{F}^\phi = -\frac{\hat{C}^u}{2}. \quad (\text{C1})$$

The system (C1) can be solved analytically, imposing that all spectra and spectral functions vanish at  $k = \infty$  (Bühler et al. 2014):

$$\hat{F}^\psi(s) = \frac{1}{2} \int_s^\infty [\hat{C}^u(\sigma) \cosh(s - \sigma) + \hat{C}^v(\sigma) \sinh(s - \sigma)] d\sigma, \quad (C2)$$

and

$$\hat{F}^\phi(s) = \frac{1}{2} \int_s^\infty [\hat{C}^u(\sigma) \sinh(s - \sigma) + \hat{C}^v(\sigma) \cosh(s - \sigma)] d\sigma, \quad (C3)$$

where we made the following change of variables

$$s \stackrel{\text{def}}{=} \log k, \quad \text{and} \quad \frac{d}{ds} = k \frac{d}{dk}. \quad (C4)$$

Contrary to Bühler et al. (2014), we use  $u$  (not  $v$ ) for the across-track velocity component.

We evaluate the integrals (C2) and (C3) numerically using Simpson's rule. Of course, we do not know  $\hat{C}^u$  and  $\hat{C}^v$  at very small scales, and we stop the integration of (C2) and (C3) short of  $\infty$ . Hence, the Bühler et al. (2014) decomposition is not very accurate at very high wavenumbers. The rotational  $\hat{K}^\psi$  and divergent  $\hat{K}^\phi$  spectra are computed from the spectral functions  $\hat{F}^\psi$  and  $\hat{F}^\phi$  and the KE spectra  $\hat{C}^u$  and  $\hat{C}^v$  (Bühler et al. 2014):

$$\hat{K}^\psi(k) = \left(1 - k \frac{d}{dk}\right) \hat{F}^\psi = \hat{F}^\psi - \hat{F}^\phi + \frac{\hat{C}^u}{2}, \quad (C5)$$

and

$$\hat{K}^\phi = \left(1 - k \frac{d}{dk}\right) \hat{F}^\phi = \hat{F}^\phi - \hat{F}^\psi + \frac{\hat{C}^v}{2}. \quad (C6)$$

For the wave–vortex decomposition, we use the Garrett–Munk spectrum (Munk 1981) to obtain the ratio  $\hat{F}_w^\psi(k)/\hat{F}_w^\phi(k)$  for the inertia–gravity waves (Bühler et al. 2014). Munk (1981) gives an empirical expression for the total energy spectrum:

$$E_{\text{GM}}(\omega, j) = E_0 B(\omega) H(j), \quad (C7)$$

where  $E_0$  is a constant;

$$B(\omega) \stackrel{\text{def}}{=} C \frac{2f}{\pi\omega} (\omega^2 - f_0^2)^{-1/2}, \quad \int_f^{N(z)} B(\omega) d\omega = 1, \quad (C8)$$

where  $C$  is a normalization constant; and

$$H(j) = \frac{(j^2 + j_*^2)^{-1}}{\sum_1^\infty (j^2 + j_*^2)^{-1}}. \quad (C9)$$

Note that Munk (1981) assumes an exponential stratification profile with  $e$ -folding vertical scale  $h$ :

$$N(z) = N_0 e^{z/h}, \quad (C10)$$

where  $N_0$  is the buoyancy frequency at the base of the mixed layer and approximates the WKB vertical wavenumber by

$$m(z) \approx \frac{\pi}{h} \frac{N(z)}{N_0} j. \quad (C11)$$

Also, in (C8)  $\omega$  is the frequency, related to the horizontal and vertical wavenumbers by the dispersion relationship

$$\omega^2(k_h^2 + m^2) = k_h^2 N^2 + m^2 f_0^2. \quad (C12)$$

We can write the GM spectrum as a function of the horizontal wavenumber  $k_h$  using the dispersion relationship

$$E_{\text{GM}}(k_h, j) = E_{\text{GM}}(\omega, j) \frac{d\omega}{dk_h}. \quad (C13)$$

To calculate the ratio  $\hat{F}^\phi/\hat{F}^\psi$ , we first notice that plane-wave inertial–gravity waves obey a simple relationship between the total energy spectrum  $E(k_h, m)$  and the spectrum of the horizontal velocity potential  $\phi$ , associated with the horizontally divergent part of the flow. The kinetic energy spectrum of inertia–gravity waves is

$$\hat{K}_w(k_h, m) = \left(1 + \frac{f_0^2}{\omega^2} + \frac{k_h^2}{m^2}\right) k_h^2 \hat{C}_w^\phi(k_h, m), \quad (C14)$$

where we used  $\hat{C}^\psi = (f_0^2/\omega^2) \hat{C}^\phi$ . The potential energy is

$$\hat{P}_w(k_h, m) = \frac{N^2}{\omega^2} \frac{k_h^4}{m^2} \hat{C}_w^\phi(k_h, m). \quad (C15)$$

Adding (C14) to (C15), and using the dispersion relationship (C12), we obtain

$$\hat{E}_w(k_h, m) = \left(1 + \frac{k_h^2}{m^2}\right) k_h^2 \hat{C}_w^\phi(k_h, m). \quad (C16)$$

Making the hydrostatic approximation (i.e., ignoring the  $k_h^2/m^2$  above) results in an error of less than 1% at scales larger than 10 km. To obtain  $\hat{F}_w^\phi(k)$  we sum on  $j$  and transform the spectra from two-dimensional,



TABLE D2. Details of the llc spin-up hierarchy. In this study, we analyze a subset of the llc 4320 simulation is analyzed.

Simulation	Resolution	Time step (s)	Period	Tides
ECCO2 adjoint method estimate	1/6°	1200	January 2009–December 2011	No
llc1080	1/12°	90	January 2010–July 2012	No
llc2160	1/24°	45	January 2011–April 2013	Yes
llc4320	1/48°	25	September 2011–December 2011	Yes

horizontally isotropic to one-dimensional spectrum (e.g., Bühler et al. 2014). We obtain

$$\hat{F}_W^\phi(k) = \frac{1}{\pi} \int_{|k|}^{\infty} \sum_j \frac{E_{\text{GM}}(k_h, j)}{k_h^2 + k_h^4/m^2} \sqrt{k_h^2 - k^2} dk_h. \quad (\text{C17})$$

Similarly,

$$\hat{F}_W^\psi(k) = \frac{1}{\pi} \int_{|k|}^{\infty} \sum_j \frac{f_0^2}{\omega^2} \frac{E_{\text{GM}}(k_h, j)}{k_h^2 + k_h^4/m^2} \sqrt{k_h^2 - k^2} dk_h. \quad (\text{C18})$$

The integrals in (C17) and (C18) are evaluated numerically using Simpson's rule. Given that the divergent component  $\hat{K}^\phi(k)$  is assumed to be only due to inertia-gravity waves,  $F^\phi(k) = F_W^\phi(k)$ , and a full wave–vortex decomposition is achieved (Bühler et al. 2014):

$$\frac{\hat{C}_W^v(k)}{2} = \frac{f_0^2}{\omega_\star^2(k)} \hat{F}^\phi - \hat{F}^\psi + \frac{\hat{C}^v}{2}, \quad (\text{C19})$$

and

$$\frac{\hat{C}_W^u(k)}{2} = \left[ 1 + k \frac{d}{dk} \left( \frac{f_0^2}{\omega_\star^2(k)} \right) \right] \hat{F}^\phi - \frac{f_0^2}{\omega_\star^2(k)} \left( \hat{F}^\psi - \frac{\hat{C}^v}{2} \right). \quad (\text{C20})$$

Equations (C19) and (C20) follow from (C1), and  $f_0^2/\omega_\star^2(k) \stackrel{\text{def}}{=} \hat{F}_W^\psi/\hat{F}_W^\phi$  (Bühler et al. 2014). Note that only  $f_0^2/\omega_\star^2(k)$  needs to be differentiated. Finally, the vortex (geostrophic flow) components are obtained by subtraction  $\hat{C}_V^u = \hat{C}^u - \hat{C}_W^u$  and  $\hat{C}_V^v = \hat{C}^v - \hat{C}_W^v$ .

## APPENDIX D

### Details of the llc 4320 Simulation

The llc4320 simulation is based on a global ocean and sea ice configuration of the Massachusetts Institute of Technology general circulation model (MITgcm; Marshall et al. 1997; Hill et al. 2007) and uses a latitude–longitude–polar cap (llc) grid (Forget et al. 2015). The MITgcm was spunup in a hierarchy of increasing horizontal resolutions with 90 vertical levels (details in Table D2). The simulation analyzed here is

the highest resolution, llc4320, with a time step of 25 s. The prognostic model variables are saved at hourly intervals. (Control files and details of the high-resolution llc model setups and forcing files are available at [http://mitgcm.org/viewvc/MITgcm/MITgcm\\_contrib/llc\\_hires/](http://mitgcm.org/viewvc/MITgcm/MITgcm_contrib/llc_hires/).)

Surface fluxes are from the 0.14° ECMWF atmospheric operational model analysis, starting 2011. The surface fields include 10-m wind velocity, 2-m air temperature and humidity, downwelling long and shortwave radiation, and atmospheric pressure load. These fields are converted to surface fluxes using the bulk formulae of Large and Yeager (2004) and the dynamic/thermodynamic sea ice model of Losch et al. (2010). The model also includes tidal forcing for the 16 most significant components that are applied as additional atmospheric pressure forcing (A. Chaudhuri 2014, personal communication).

## APPENDIX E

### Linear Stability Analysis

We perform a standard local and linear quasigeostrophic stability analysis (e.g., Tulloch et al. 2011) to a base state derived from the cDrake experiment (Chereskin et al. 2012; see Fig. E1). The velocity profile is a 4-yr time mean estimated at a location in the Polar Front in Drake Passage from daily objective maps of geostrophic velocity using a two-dimensional array of current- and pressure-recording inverted echo sounders from the cDrake experiment (Firing et al. 2014). The buoyancy profile is a 4-yr time-mean at the same location from daily maps of acoustic travel time. An empirical lookup table of hydrographic properties constructed from nearly 600 CTD and Argo profiles in the cDrake region is used to convert the mean travel time to a corresponding buoyancy profile (Chidichimo et al. 2014).

The structure of the growth rate curves is roughly aligned with the mean velocity profile (Fig. E2). The most unstable has a wavelength of about 188 km, with a growth rate of about  $0.17 \text{ day}^{-1}$ . These instabilities are Phillips-like modes (e.g., Tulloch et al. 2011) associated

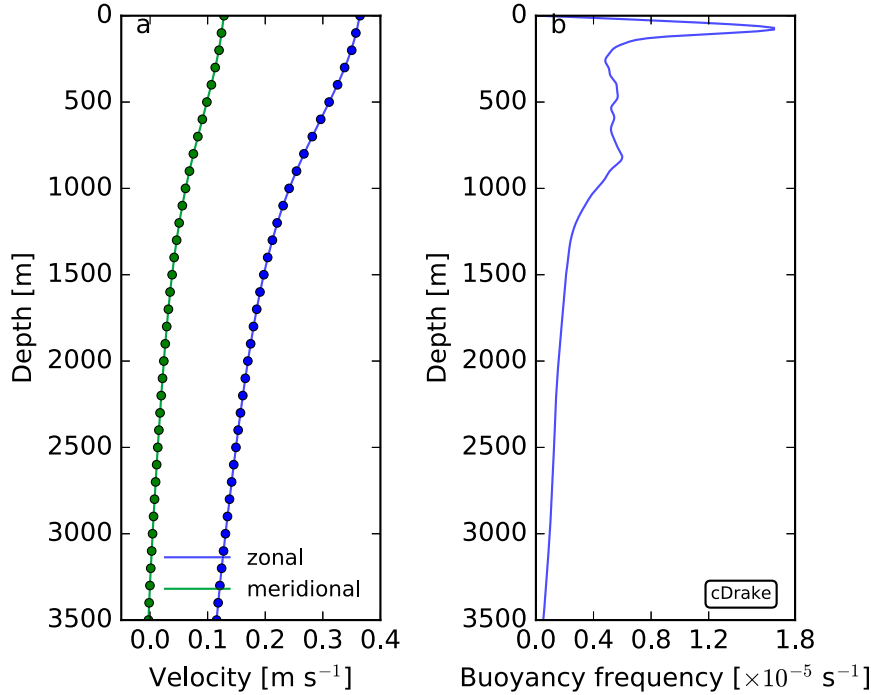


FIG. E1. Base state used in the linear stability calculations.

with a deep sign reversal of the background potential vorticity gradient.

## APPENDIX F

### Depth Dependence of SQG KE Spectra for Drake Passage Stratification

The vertical structure of SQG solutions  $\chi(z; k_h)$  is governed by (e.g., LaCasce 2012)

$$\frac{d}{dz} \left[ \frac{f_0^2}{N^2(z)} \frac{d\chi}{dz} \right] - k_h^2 \chi = 0, \quad (\text{F1})$$

subject to inhomogeneous Neumann boundary conditions at the surface that represent surface buoyancy variations:

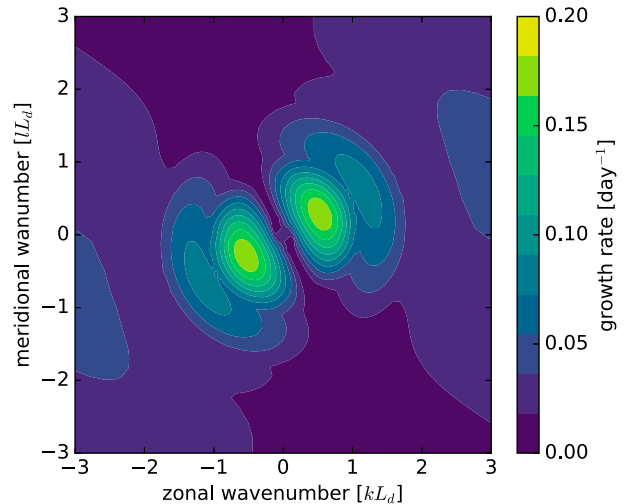
$$\frac{d\chi}{dz} = 1 \quad \text{at} \quad z = 0. \quad (\text{F2})$$

We assume zero buoyancy anomalies at the bottom:

$$\frac{d\chi}{dz} = 0 \quad \text{at} \quad z = -H, \quad (\text{F3})$$

where  $k_h = \sqrt{k^2 + l^2}$  is the magnitude of the horizontal wavenumber, and  $N(z)/f_0$  is the local stratification/inertial frequency.

We generate a SQG-like surface KE spectrum and use the SQG vertical structure  $F(z; k_h)$  to investigate its vertical structure. The SQG vertical structure  $F(z; k_h)$  is computed by solving (F1)–(F2)–(F3) using a second-order finite difference scheme. We use the average in situ stratification based on 76 top to bottom CTD profiles from the cDrake experiment (Chereskin et al. 2012). As expected, the KE spectrum steepens at depth (LaCasce 2012). For instance, the KE spectra in the 10–50-km

FIG. E2. Growth rate in horizontal wavenumber space. The wavenumbers are normalized by the deformation scale ( $2\pi \times 16$  km).

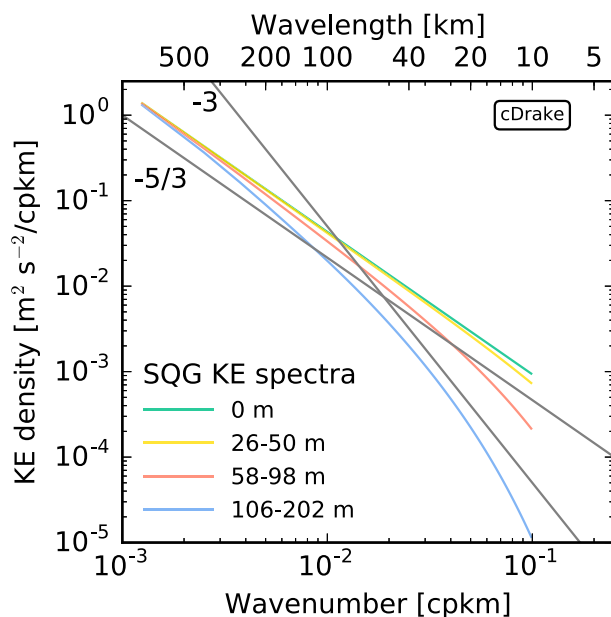


FIG. F1. Depth dependence of SQG-like KE spectra in the range of scales resolved by the ADCP data. The surface spectra follow a  $k_h^{-5/3}$  power law. The vertical dependence is computed from the SQG solution's vertical structure for each  $k_h$  given the global average stratification from the cDrake experiment. Colors represent spectra in different layers used in computing the ADCP and llc4320 spectral estimates.

subrange approximately follow a power law between  $k_h^{-2}$  and  $k_h^{-3}$  in the 106–202-m layer (Fig. F1).

In summary, a small (but systematic) steepening in KE spectrum would be present in the upper 200 m if SQG flows dominated the upper-ocean variability in Drake Passage. Both ADCP and model KE spectra lack such systematic depth dependence (see sections 3 and 6) and therefore are inconsistent with predictions of SQG turbulence.

#### REFERENCES

- Bendat, J., and A. Piersol, 2010: *Random Data: Analysis and Measurement Procedures*. 4th ed. Wiley, 604 pp.
- Biol, F., M. Canet, and C. Estournel, 2010: Aspects of the seasonal variability of the Northern Current (NW Mediterranean Sea) observed by altimetry. *J. Mar. Syst.*, **81**, 297–311, doi:10.1016/j.jmarsys.2010.01.005.
- Blumen, W., 1978: Uniform potential vorticity flow: Part II. A model of wave interactions. *J. Atmos. Sci.*, **35**, 784–789, doi:10.1175/1520-0469(1978)035<0784:UPVFP>2.0.CO;2.
- Bryden, H. L., 1979: Poleward heat flux and conversion of available potential energy in Drake Passage. *J. Mar. Res.*, **37**, 1–22.
- Bühler, O., J. Callies, and R. Ferrari, 2014: Wave–vortex decomposition of one-dimensional ship-track data. *J. Fluid Mech.*, **756**, 1007–1026, doi:10.1017/jfm.2014.488.
- Callies, J., and R. Ferrari, 2013: Interpreting energy and tracer spectra of upper-ocean turbulence in the submesoscale range (1–200 km). *J. Phys. Oceanogr.*, **43**, 2456–2474, doi:10.1175/JPO-D-13-063.1.
- , —, J. Klymak, and J. Gula, 2015: Seasonality in submesoscale turbulence. *Nat. Commun.*, **6**, 6862, doi:10.1038/ncomms7862.
- Capet, X., J. C. McWilliams, M. J. Molemaker, and A. F. Shchepetkin, 2008: Mesoscale to submesoscale transition in the California Current System. Part III: Energy balance and flux. *J. Phys. Oceanogr.*, **38**, 2256–2269, doi:10.1175/2008JPO3810.1.
- Charney, J., 1971: Geostrophic turbulence. *J. Atmos. Sci.*, **28**, 1087–1095, doi:10.1175/1520-0469(1971)028<1087:GT>2.0.CO;2.
- Chereskin, T. K., K. A. Donohue, and D. R. Watts, 2012: cDrake: Dynamics and transport of the Antarctic Circumpolar Current in Drake Passage. *Oceanography*, **25**, 134–135, doi:10.5670/oceanog.2012.86.
- Chidichimo, M. P., K. A. Donohue, D. R. Watts, and K. L. Tracey, 2014: Baroclinic transport time series of the Antarctic Circumpolar Current measured in Drake Passage. *J. Phys. Oceanogr.*, **44**, 1829–1853, doi:10.1175/JPO-D-13-071.1.
- Dibarboure, G., F. Boy, J. D. Desjonqueres, S. Labroue, Y. Lasne, N. Picot, J. C. Poisson, and P. Thibaut, 2014: Investigating short-wavelength correlated errors on low-resolution mode altimetry. *J. Atmos. Oceanic Technol.*, **31**, 1337–1362, doi:10.1175/JTECH-D-13-00081.1.
- Durand, F., D. Shankar, F. Birol, and S. S. C. Shenoi, 2008: An algorithm to estimate coastal currents from satellite altimetry: A case study for the East India Coastal Current. *J. Oceanogr.*, **64**, 831–845, doi:10.1007/s10872-008-0069-2.
- Egbert, G. D., A. F. Bennett, and M. G. G. Foreman, 1994: TOPEX/POSEIDON tides estimated using a global inverse model. *J. Geophys. Res.*, **99**, 24 821–24 852, doi:10.1029/94JC01894.
- Faugere, Y., J. Dorandeu, F. Lefevre, N. Picot, and P. Femenias, 2006: Envisat ocean altimetry performance assessment and cross-calibration. *Sensors*, **6**, 100–130, doi:10.3390/s6030100.
- Ferrari, R., and C. Wunsch, 2010: The distribution of eddy kinetic and potential energies in the global ocean. *Tellus*, **62A**, 92–108, doi:10.3402/tellusa.v62i2.15680.
- Firing, E., J. M. Hummon, and T. K. Chereskin, 2012: Improving the quality and accessibility of current profile measurements in the Southern Ocean. *Oceanography*, **25**, 164–165, doi:10.5670/oceanog.2012.91.
- Firing, Y. L., T. K. Chereskin, and M. R. Mazloff, 2011: Vertical structure and transport of the Antarctic Circumpolar Current in Drake Passage from direct velocity observations. *J. Geophys. Res.*, **116**, C08015, doi:10.1029/2011JC006999.
- , —, D. R. Watts, K. L. Tracey, and C. Provost, 2014: Computation of geostrophic streamfunction, its derivatives, and error estimates from an array of CPIES in Drake Passage. *J. Atmos. Oceanic Technol.*, **31**, 656–680, doi:10.1175/JTECH-D-13-00142.1.
- Forget, G., J.-M. Campin, P. Heimbach, C. N. Hill, R. M. Ponte, and C. Wunsch, 2015: ECCO version 4: An integrated framework for non-linear inverse modeling and global ocean state estimation. *Geosci. Model Dev.*, **8**, 3071–3104, doi:10.5194/gmd-8-3071-2015.
- Hill, C., D. Menemenlis, B. Ciotti, and C. Henze, 2007: Investigating solution convergence in a global ocean model using a 2048-processor cluster of distributed shared memory machines. *Sci. Program.*, **15**, 107–115, doi:10.1155/2007/458463.
- Holte, J., and L. Talley, 2009: A new algorithm for finding mixed layer depths with applications to Argo data and Subantarctic Mode Water formation. *J. Atmos. Oceanic Technol.*, **26**, 1920–1939, doi:10.1175/2009JTECHO543.1.
- , J. Gilson, L. Talley, and D. Roemmich, 2010: Argo mixed layers. Accessed 15 March 2015. [Available online at <http://mixedlayer.ucsd.edu>.]

- LaCasce, J. H., 2012: Surface quasigeostrophic solutions and baroclinic modes with exponential stratification. *J. Phys. Oceanogr.*, **42**, 569–580, doi:[10.1175/JPO-D-11-0111.1](https://doi.org/10.1175/JPO-D-11-0111.1).
- Large, W. G., and S. G. Yeager, 2004: Diurnal to decadal global forcing for ocean and sea-ice models: The datasets and flux climatologies. NCAR Tech. Note TN-460+STR, 105 pp.
- Lenn, Y.-D., and T. K. Chereskin, 2009: Observations of Ekman currents in the Southern Ocean. *J. Phys. Oceanogr.*, **39**, 768–778, doi:[10.1175/2008JPO3943.1](https://doi.org/10.1175/2008JPO3943.1).
- , —, J. Sprintall, and E. Firing, 2007: Mean jets, mesoscale variability and eddy momentum fluxes in the surface layer of the Antarctic Circumpolar Current in Drake Passage. *J. Mar. Res.*, **65**, 27–58, doi:[10.1357/002224007780388694](https://doi.org/10.1357/002224007780388694).
- Le Traon, P. Y., P. Klein, B. L. Hua, and G. Dibarboure, 2008: Do altimeter wavenumber spectra agree with the interior or surface quasigeostrophic theory? *J. Phys. Oceanogr.*, **38**, 1137–1142, doi:[10.1175/2007JPO3806.1](https://doi.org/10.1175/2007JPO3806.1).
- Losch, M., D. Menemenlis, P. Heimbach, J.-M. Campin, and C. Hill, 2010: On the formulation of sea-ice models. Part 1: Effects of different solver implementations and parameterizations. *Ocean Modell.*, **33**, 129–144, doi:[10.1016/j.ocemod.2009.12.008](https://doi.org/10.1016/j.ocemod.2009.12.008).
- Marshall, J., A. Adcroft, C. Hill, L. Perelman, and C. Heisey, 1997: A finite-volume, incompressible Navier Stokes model for studies of the ocean on parallel computers. *J. Geophys. Res.*, **102**, 5753–5766, doi:[10.1029/96JC02775](https://doi.org/10.1029/96JC02775).
- Munk, W., 1981: Internal waves and small-scale processes. *Evolution of Physical Oceanography: Scientific Surveys in Honor of Henry Stommel*, B. A. Warren and C. Wunsch, Eds., MIT Press, 264–291.
- Nowlin, W. D., T. Whitworth III, and R. D. Pillsbury, 1977: Structure and transport of the Antarctic Circumpolar Current at Drake Passage from short-term measurements. *J. Phys. Oceanogr.*, **7**, 788–802, doi:[10.1175/1520-0485\(1977\)007<0788:SATOTA>2.0.CO;2](https://doi.org/10.1175/1520-0485(1977)007<0788:SATOTA>2.0.CO;2).
- Pawlowicz, R., B. Beardsley, and S. Lentz, 2002: Classical tidal harmonic analysis including error estimates in MATLAB using T-TIDE. *Comput. Geosci.*, **28**, 929–937, doi:[10.1016/S0098-3004\(02\)00013-4](https://doi.org/10.1016/S0098-3004(02)00013-4).
- Pinkel, R., 2014: Vortical and internal wave shear and strain. *J. Phys. Oceanogr.*, **44**, 2070–2092, doi:[10.1175/JPO-D-13-090.1](https://doi.org/10.1175/JPO-D-13-090.1).
- RD Instruments, 1996: Acoustic Doppler current profiler principles of operation: A practical primer. RD Instruments Tech. Rep. P/N 951-6069-00, 57 pp.
- Richman, J. G., B. K. Arbic, J. F. Shriver, E. J. Metzger, and A. J. Wallcraft, 2012: Inferring dynamics from the wavenumber spectra of an eddying global ocean model with embedded tides. *J. Geophys. Res.*, **117**, C12012, doi:[10.1029/2012JC008364](https://doi.org/10.1029/2012JC008364).
- Roblou, L., and Coauthors, 2011: Post-processing altimeter data towards coastal applications and integration into coastal models. *Coastal Altimetry*, S. Vignudelli et al., Eds., Springer, 217–246.
- Roemmich, D., and J. Gilson, 2009: The 2004–2008 mean and annual cycle of temperature, salinity, and steric height in the global ocean from the Argo program. *Prog. Oceanogr.*, **82**, 81–100, doi:[10.1016/j.pocean.2009.03.004](https://doi.org/10.1016/j.pocean.2009.03.004).
- Rudnick, D. L., and R. E. Davis, 2003: Red noise and regime shifts. *Deep-Sea Res.*, **50**, 691–699, doi:[10.1016/S0967-0637\(03\)00053-0](https://doi.org/10.1016/S0967-0637(03)00053-0).
- Sallée, J. B., K. Speer, and R. Morrow, 2008: Response of the Antarctic Circumpolar Current to atmospheric variability. *J. Climate*, **21**, 3020–3039, doi:[10.1175/2007JCLI1702.1](https://doi.org/10.1175/2007JCLI1702.1).
- Salmon, R., 1998: *Lectures on Geophysical Fluid Dynamics*. Oxford University Press, 378 pp.
- Sasaki, H., P. Klein, B. Qiu, and Y. H. Sasai, 2014: Impact of oceanic-scale interactions on the seasonal modulation of ocean dynamics by the atmosphere. *Nat. Commun.*, **5**, 5636, doi:[10.1038/ncomms6636](https://doi.org/10.1038/ncomms6636).
- Shcherbina, A. Y., E. A. D’Asaro, C. M. Lee, J. M. Klymak, M. J. Molemaker, and J. C. McWilliams, 2013: Statistics of vertical vorticity, divergence, and strain in a developed submesoscale turbulence field. *Geophys. Res. Lett.*, **40**, 4706–4711, doi:[10.1002/grl.50919](https://doi.org/10.1002/grl.50919).
- Smith, J. A., 2008: Vorticity and divergence of surface velocities near shore. *J. Phys. Oceanogr.*, **38**, 1450–1468, doi:[10.1175/2007JPO3865.1](https://doi.org/10.1175/2007JPO3865.1).
- Stephenson, G. R., Jr., S. T. Gille, and J. Sprintall, 2012: Seasonal variability of upper-ocean heat content in Drake Passage. *J. Geophys. Res.*, **117**, C04019, doi:[10.1029/2011JC007772](https://doi.org/10.1029/2011JC007772).
- Thomas, L., A. Tandon, and A. Mahadevan, 2008: Submesoscale processes and dynamics. *Ocean Modeling in an Eddying Regime*, *Geophys. Monogr.*, Vol. 177, Amer. Geophys. Union, 17–38.
- Tulloch, R., J. Marshall, C. Hill, and K. S. Smith, 2011: Scales, growth rates, and spectral fluxes of baroclinic instability in the ocean. *J. Phys. Oceanogr.*, **41**, 1057–1076, doi:[10.1175/2011JPO4404.1](https://doi.org/10.1175/2011JPO4404.1).
- Verron, J., and Coauthors, 2015: The SARAL/AltiKa altimetry satellite mission. *Mar. Geod.*, **38**, 2–21, doi:[10.1080/01490419.2014.1000471](https://doi.org/10.1080/01490419.2014.1000471).
- Wang, D., C. N. Flagg, K. Donohue, and H. T. Rossby, 2010: Wavenumber spectrum in the Gulf Stream from shipboard ADCP observations and comparison with altimetry measurements. *J. Phys. Oceanogr.*, **40**, 840–844, doi:[10.1175/2009JPO4330.1](https://doi.org/10.1175/2009JPO4330.1).
- Wunsch, C., 2013: Baroclinic motions and energetics as measured by altimeters. *J. Atmos. Oceanic Technol.*, **30**, 140–150, doi:[10.1175/JTECH-D-12-00035.1](https://doi.org/10.1175/JTECH-D-12-00035.1).
- Xu, Y., and L.-L. Fu, 2012: The effects of altimeter instrument noise on the estimation of the wavenumber spectrum of sea surface height. *J. Phys. Oceanogr.*, **42**, 2229–2233, doi:[10.1175/JPO-D-12-0106.1](https://doi.org/10.1175/JPO-D-12-0106.1).
- Zhou, X.-H., D.-P. Wang, and D. Chen, 2015: Global wavenumber spectrum with corrections for altimeter high-frequency noise. *J. Phys. Oceanogr.*, **45**, 495–503, doi:[10.1175/JPO-D-14-0144.1](https://doi.org/10.1175/JPO-D-14-0144.1).